

UNIVERSIDADE DE SANTIAGO DE  
COMPOSTELA



FACULTADE DE FÍSICA

Departamento de Física de Partículas

Pulse-shape analysis of signals from a  
CALIFA scintillator prototype fired by  
photons and light charged particles and its  
application to PID.

Memoria presentada por:  
**Diego Ramos Doval**  
como Trabajo Fin de Máster dentro del  
Máster Oficial de Física Nuclear  
y de Partículas y sus aplicaciones  
tecnológicas y médicas.  
Junio 2012



# **UNIVERSIDADE DE SANTIAGO DE COMPOSTELA**

El Doctor Héctor Álvarez Pol, Profesor del Departamento de Física de Partículas de la Universidad de Santiago de Compostela,

## **INFORMA:**

que la memoria titulada **Pulse-shape analysis of signals from a CALIFA scintillator prototype fired by photons and light charged particles and its application to PID** ha sido realizada bajo su dirección por **Diego Ramos Doval** en el **Departamento de Física de Partículas de esta Universidad**, y constituye el **Trabajo de Fin de Máster** que presenta para optar al **Grado de Máster en Física Nuclear y de Partículas y sus aplicaciones científicas y médicas**.

Santiago de Compostela, a 20 de Junio de 2012.

Fdo. Héctor Álvarez Pol

Fdo. Diego Ramos Doval



# Contents

<b>1</b>	<b>Introduction</b>	<b>1</b>
<b>2</b>	<b>The detection bases</b>	<b>3</b>
2.1	Passage of particles through matter . . . . .	3
2.1.1	Energy loss of charged particles . . . . .	4
2.1.2	Energy loss of gamma rays . . . . .	7
2.2	Scintillation detectors . . . . .	11
2.2.1	Scintillation detector principles . . . . .	12
2.2.2	Light output response . . . . .	14
<b>3</b>	<b>CALIFA</b>	<b>17</b>
3.1	Goals of CALIFA . . . . .	18
3.2	CsI(Tl) scintillation crystals in CALIFA . . . . .	18
3.2.1	Scintillation mechanism in inorganic crystals with activators . . . . .	19
3.2.2	CsI(Tl) emission espectrum . . . . .	21
<b>4</b>	<b>Experimental Setup</b>	<b>23</b>
4.1	ProtoZero, first step towards CALIFA . . . . .	23
4.2	General features . . . . .	23
4.3	Different readout systems . . . . .	26
4.4	Avalanche photodiode . . . . .	28
<b>5</b>	<b>Data Analysis</b>	<b>31</b>
5.1	Binomial smoothing filter . . . . .	31
5.2	Moving Window Deconvolution . . . . .	32
5.3	Baseline subtraction . . . . .	35
5.4	Energy Calibration . . . . .	37
5.5	Pulse Shape Analysis for PID . . . . .	41
5.5.1	Signal Rise Time . . . . .	42
5.5.2	Fast & Slow Components . . . . .	44

<b>6</b>	<b>Results</b>	<b>53</b>
<b>7</b>	<b>Summary and Conclusions</b>	<b>59</b>
<b>A</b>	<b>Moving Window Deconvolution Calculations</b>	<b>61</b>
<b>B</b>	<b>Calculations for Fast and Slow components deduction</b>	<b>63</b>
B.1	MWD with length $L_1$ . . . . .	63
B.2	Derivative of MWD ( $L_1$ ) and multiplication by $e^{\frac{t}{\tau_s}}$ . . . . .	64
B.3	MWD with length $L_2 < L_1$ . . . . .	65

# Chapter 1

## Introduction

CALIFA (Calorimeter for In-Flight emitted gAmmas and light charged particles) is an electromagnetic calorimeter for the  $R^3B$  (Reactions with Relativistic Radioactive Beams) setup at the new Facility for Antiproton and Ion Research (FAIR), which will be built at GSI Darmstadt. It is intended to detect gamma rays, protons and light nuclei emitted from the de-excitation of the reaction products in the target region. Among its requirements, a good energy resolution over a considerable dynamical range (some keV up to several 100 MeV), a large full energy efficiency and some particle identification capability are remarkable.

A small prototype of the detector, known as *ProtoZero* and composed of 13 CsI(Tl) crystals, featuring a newly developed digital data acquisition was tested with a heavy-ion beam in the experimental cave C at GSI in November 2010. The goals were to test the energy resolution of the crystals, a set of particle identification algorithms and the data acquisition with a newly developed FPGA-based, embedded real-time data analysis.

The aim of this work is studying the characteristics of the signals obtained with the *ProtoZero* crystals and electronics associated in order to find the parameters suitable for determining the energy deposited by the incident particles, as well as for identifying these particles. To perform this task, the ProtoZero was part of a set of detectors installed to study the reactions produced when a pulsed  $^{197}\text{Au}^{65+}$  beam of  $E = 400$  AMeV impinged upon a Pb target. A full pulse shape analysis of signals coming from one of the crystals of the *ProtoZero* has been made, using an Avalanche PhotoDiode (APD) as photon-electron converter, and processing and storing the signals with a shaper amplifier and a fast-ADC.

The identification will be based on two methods. The risetime of the signal provides information about the particle which produces the signal. The relation between the two components in which the signal can be divided,

the *fast* and *slow* components, could also serve for the identification. A crosscheck is obtained using both methods.

This procedure needs a previous treatment of the signal, a binomial filter developed for removing high frequency noise, and an algorithm, named *Moving Window Deconvolution (MWD)*, built for separating electronic contributions from the original signal.

This work is divided in five chapters. In the first chapter the bases for the detection in the CALIFA calorimeter, the energy loss for the different types of light particles and the scintillation principles are explained. In the next chapter the basic characteristics of CALIFA detector and the properties of its scintillation crystals are shown. In chapter 4 the setup of the experiment is exhibited, highlighting the different readout systems and the photodetector *photodiode*. In chapter 5 the complete analysis carried out in this work including the first results is developed. In chapter 6 the results obtained in the previous analysis are shown. These results prove the power of both methods in order to achieve particle identification. In chapter 7 a summary of the work and the conclusions obtained are presented.

# Chapter 2

## The detection bases

An electromagnetic calorimeter is a detector capable to measure the energy deposition caused by a contained electromagnetic shower initiated by an incident particle.

Electromagnetic calorimeters are traditionally classified in one of the two following categories: homogeneous and sampling electromagnetic calorimeters. A sampling calorimeter consists of an active medium which generates a signal, and a passive medium which works as absorber. In an homogeneous calorimeter, the entire volume is sensitive and contributes to the signal. Homogeneous electromagnetic calorimeters may be built with inorganic heavy (high-Z) scintillating crystals such as BGO, CsI, NaI, and PWO, non-scintillating Cherenkov radiators such as lead glass and lead fluoride, or ionizing noble liquids.

The electromagnetic shower detected by the calorimeters will depend on the calorimeter development, but also on how particles interact with matter. In this chapter I will explain the main interactions that particles suffer when they cross through matter, and how they lose their energy. Additionally, I will explain the scintillation fundamentals, which are the bases for the onwards analysis.

### 2.1 Passage of particles through matter

The operation of any radiation detector basically depends on the manner in which the radiation to be detected interacts with the material of the detector itself. An understanding of the response of a specific type of detector must therefore be based on a familiarity with the fundamental mechanisms by which radiations interact and lose their energy in matter. In all cases of practical interest, the interaction results in the full or partial transfer of en-

ergy of the incident radiation to electrons or nuclei of the constituent atoms, or to charged particle products of nuclear reactions. For charged particles and photons, the most common process are by far the electromagnetic interactions, in particular, inelastic collisions with the atomic electrons. This is not too surprising considering the strength and long range of the Coulomb force relative to the other interactions. The type of processes allowed to each type of radiation explain, among other things, their penetrability through matter. In this section, the principles of energy depositon on matter of charged particles and photons are presented.

### 2.1.1 Energy loss of charged particles

For charged particles, it is necessary to separate particles into two clases, electrons and positrons on the one hand, and charged particles heavier than electrons on the other hand.

Heavy charged particles, such as the alpha particle, interact with matter primarily through Coulomb forces between their charge and the negative charge of the orbital electrons within the absorber atoms. Although interactions of the particle with nuclei are also possible, such encounters occur only rarely, and are not normally significant in the response of radiation detectors.

Absorbing medium electrons feel an impulse from the attractive or repulsive Coulomb force as the particle passes its vicinity. Depending on the proximity of the encounter, this impulse may be sufficient either to raise the electron to a higher shell within the absorber atom, (*excitation*), or to remove completely the electron from the atom, (*ionization*). The maximum energy that can be transferred from a charged particle of mass  $m$  with kinetic energy  $T$  to an electron of mass  $m_0$  in a single collision is  $4Tm_0/m$  [3]. This small fraction of the total energy makes that the primary particle loses its energy in many interactions. At any given time, the particle is interacting with many electrons, so the net effect is to decrease its velocity continuously until the particle is stopped.

For particles with a given charge, its *specific energy loss* increases as the particle velocity is decreased. The classical expression that describes this specific energy loss is known as the *Bethe formula*[3]

$$-\frac{dE}{dx} = \frac{4\pi e^4 z^2}{m_0 v^2} N B \quad (2.1)$$

where

$$B = Z \left[ \ln \frac{2m_0 v^2}{I} - \ln \left( 1 - \frac{v^2}{c^2} \right) - \frac{v^2}{c^2} \right] \quad (2.2)$$

In these expressions,  $v$  and  $ze$  are the velocity and charge of the primary particle,  $N$  and  $Z$  are the number density and atomic number of the absorber atoms,  $m_o$  is the electron rest mass. Finally the parameter  $I$  represents the average excitation and ionization potential of the absorber.

When comparing different charged particles of the same velocity, the only factor that may change outside the logarithmic term in the last equation is  $z^2$ , which means that particles with the greatest charge will have the largest specific energy loss. For a given particle, the specific energy loss varies as  $1/v^2$ . This behavior can be explained by the fact that the charged particle spends a greater time in the vicinity of any given electron when its velocity is low, so the energy transfer is larger. In Fig. 2.1 how the specific energy loss changes as a function of energy for different charged particles is shown.

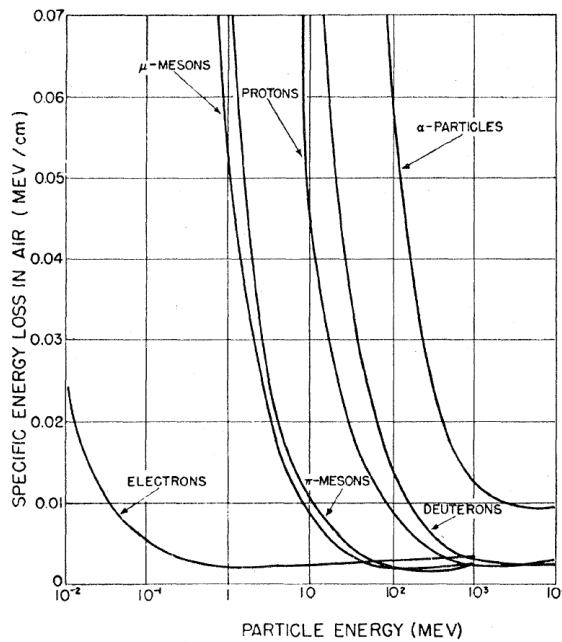


Figure 2.1: Variation of the energy loss in air versus energy of the charged particle. Picture taken from [4].

The plot of the specific energy loss along the track of a charged particle is known as the *Bragg curve*. An example of this curve is shown in figure 2.2 for alphas of 5.49 MeV, where we can see how most of energy is deposited just before stopping, in the so-called Bragg peak.

With respect to fast electrons, they lose their energy at a lower rate and follow a much more tortuous path through absorbing materials when compared with heavy charged particles. Large deviations in the electron path

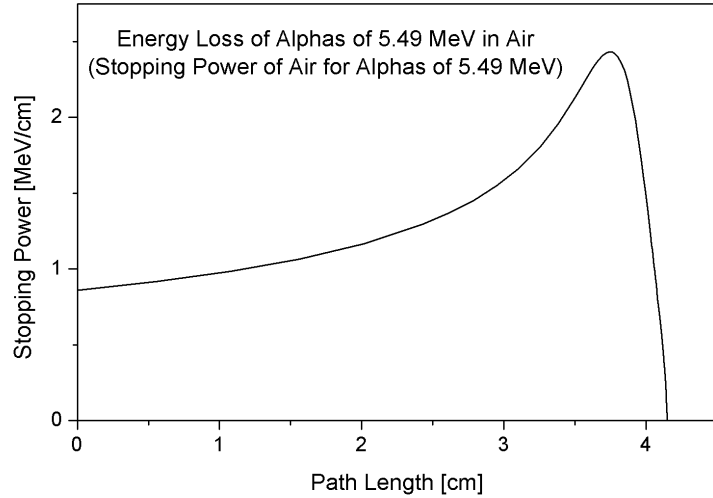


Figure 2.2: The especific energy loss along an alpha track. The loss is higher just at the end of the track.

are now possible because its mass is equal to that of the orbital electrons with which it is interacting, and a much larger fraction of its energy can be lost in a single encounter.

A similar expression is possible to be derived by Bethe to describe the specific energy loss due to ionization and excitation for fast electrons [4]

$$-\frac{dE}{dx} = \frac{2\pi e^4 N Z}{m_0 v^2} \left( \ln \frac{m_0 v^2 E}{2I^2(1 - \beta^2)} - \ln 2 \left( 2\sqrt{1 - \beta^2} - 1 + \beta^2 \right) \right. \\ \left. + (1 - \beta^2) + \frac{1}{8} \left( 1 - \sqrt{1 - \beta^2} \right)^2 \right) \quad (2.3)$$

Electrons also differ from heavy charged particles in that some energy may be lost by radiative processes as well as by Coulomb interactions. These radiative losses take the form of *bremsstrahlung* or electromagnetic radiation, which can emanate from any position along the electron track. The linear specific energy loss through this radiative process is [4]

$$-\frac{dE}{dx} = \frac{NEZ(Z+1)e^4}{137m_0^2c^4} \left( 4\ln \frac{2E}{m_0 c^2} - \frac{4}{3} \right) \quad (2.4)$$

The total linear stopping power for electrons is the sum of the collisional and radioactive losses.

The factors  $E$  and  $Z^2$  in the last equation show that radiative losses are more important for high electron energies and for absorber materials of large atomic number. For typical electron energies, the average bremsstrahlung photon energy is quite low and is therefore normally reabsorbed fairly close to its point of origin. In some cases, however, the escape of bremsstrahlung can influence the response of small detectors.

In the figure 2.3 a comparison of how different particles lose their energy in a given material (water in this case) is shown. Electrons lose energy in a gradual way with the depth, and compared to heavier charged particles, their range is smaller.

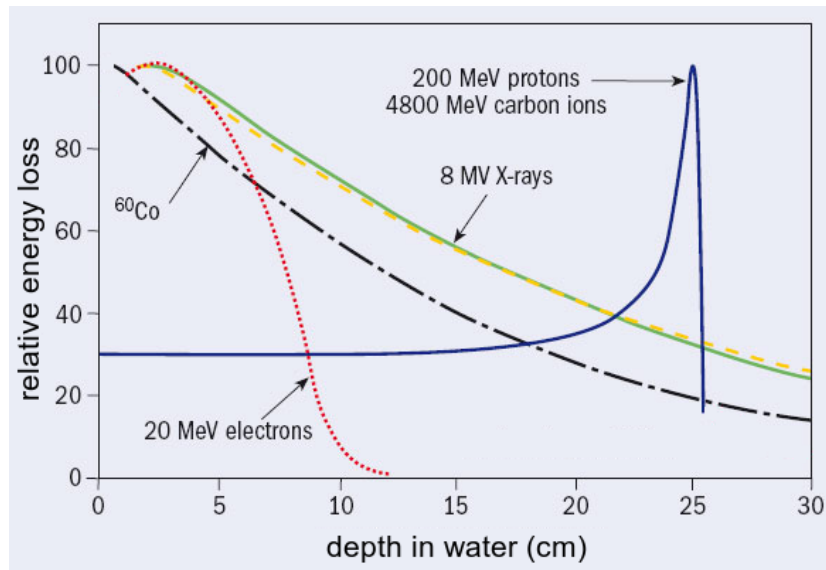


Figure 2.3: Comparison of energy loss in water for different particles. The specific case of  $^{60}\text{Co}$  which is one of the most widely used source of gamma rays is shown.

### 2.1.2 Energy loss of gamma rays

Although a large number of possible interaction mechanisms are known for gamma rays in matter, only three major types play an important role in radiation measurements: *photoelectric effect*, *Compton scattering*, and *pair production*. All these processes lead to the partial or complete transfer of the gamma-ray photon energy to electron energy. The main difference in the interaction of gamma rays with respect to charged particles is that here the history of the photons changes suddenly in each interaction, in that the photon either disappears entirely or is scattered through a significant angle.

### **Photoelectric effect**

The photoelectric effect involves the absorption of a photon by an atomic electron, with the subsequent ejection of the electron from the atom. The energy of the outgoing electron is then

$$E = h\nu - E_0 \quad (2.5)$$

where  $E_0$  is the binding energy of the electron.

Since a free electron cannot absorb a photon and also conserve momentum, the photoelectric effect always occurs on bound electrons with the nucleus absorbing the recoil momentum, and so the photoelectron carries off the majority of the original photon energy.

In addition to the photoelectron, the interaction also creates an ionized atom with a vacancy in one of its bound shells. This vacancy is quickly filled through capture of a free electron or rearrangement of electrons from other shells of the atom. Therefore, one or more characteristic X-ray are reabsorbed close to the original site through photoelectric absorption. In some cases, the emission of an Auger electron may substitute for the characteristic X-ray in carrying away the atomic excitation energy.

No single analytic expression is valid for the probability of photoelectric absorption per atom over all ranges of  $E_\gamma$  and Z, but a rough approximation is [11]

$$\tau = \text{constant} \times \frac{Z^n}{E_\gamma^{3.5}} \quad (2.6)$$

where  $4 \leq n \leq 5$

This severe dependence on the gamma energy and atomic number of the absorber makes the photoelectric effect the predominant mode of interaction for gamma rays of relatively low energy and in materials of high atomic number.

### **Compton scattering**

Compton scattering is probably one of the best understood processes in photon interactions. This is the scattering of photons on free electrons. In matter, the electrons are bound. However, if the photon energy is high with respect to the binding energy, this latter energy can be ignored and the electrons can be considered as essentially free.

Figure 2.4 illustrates this scattering process. The incoming gamma ray photon is deflected through an angle  $\psi$  with respect to its original direction, and the photon transfers a portion of its energy to the electron. Applying

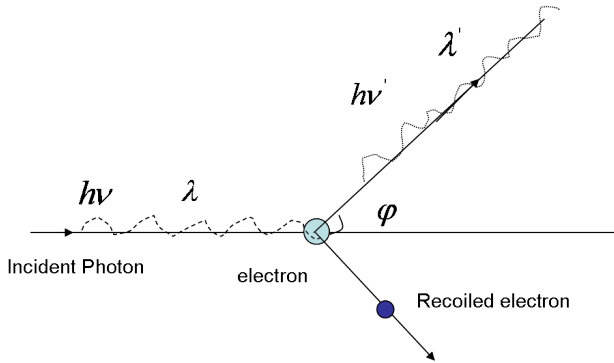


Figure 2.4: Compton scattering kinematics.

energy and momentum conservation, the following relations can be obtained.

$$h\nu' = \frac{h\nu}{1 + \frac{h\nu}{m_0c^2}(1 - \cos\psi)} \quad (2.7)$$

$$T = h\nu - h\nu' = h\nu \frac{\frac{h\nu}{m_0c^2}(1 - \cos\psi)}{1 + \frac{h\nu}{m_0c^2}(1 - \cos\psi)} \quad (2.8)$$

where  $m_0c^2$  is the rest-mass energy of the electron.

Because all angles of scattering are possible, the energy transferred to the electron can vary from zero to a large fraction of the gamma ray energy. For small scattering angles, very little energy is transferred. Some of the original energy is always retained by the incident photon, even in the extreme of  $\psi = \pi$ .

The probability of Compton scattering per atom of the absorber depends on the number of electrons available as scattering targets and therefore increases linearly with Z. The dependence on gamma ray energy is illustrated in Fig. 2.5 for the case of carbon as absorber.

The angular distribution of scattered gamma rays is predicted by the *Klein-Nishina formula* for the differential scattering cross section [3]

$$\frac{d\sigma}{d\Omega} = \frac{r_0^2}{2} \frac{1}{[1 + \gamma(1 - \cos\theta)]^2} \left( 1 + \cos^2\theta + \frac{\gamma^2(1 - \cos\theta)^2}{1 + \gamma(1 - \cos\theta)} \right) \quad (2.9)$$

where  $r_0$  is the classical electron radius. The angular distribution through this formula shows a strong tendency for forward scattering at high values of the gamma ray energy.

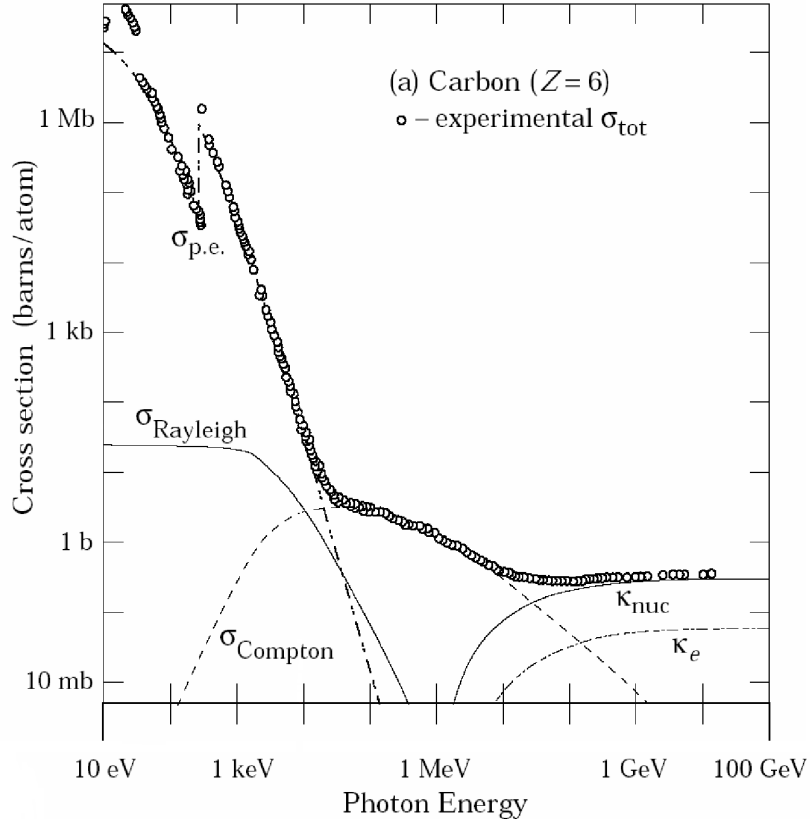


Figure 2.5: Energy dependence of the cross section for different gamma ray interaction processes in carbon.

### Pair production

The process of pair production involves the transformation of a photon into an electron-positron pair. In order to conserve momentum, this can only occur in the presence of a third body, usually a nucleus. Moreover, to create the pair, the photon must have at least an energy of 1.022 MeV. As a practical matter, the probability of this interaction remains very low until the gamma ray energy approaches several MeV and therefore pair production is predominantly confined to high energy gamma rays. All the excess energy goes into kinetic energy shared by the positron and the electron. Because the positron will subsequently annihilate after slowing down in the absorbing medium, two annihilation photons are normally produced as secondary products of the interaction.

No simple expression exists for the probability of pair production per

nucleus, but its magnitude varies approximately as the square of the absorber atomic number.

The response to gamma photons of a real detector, where all possible interactions for a definite energy are bound to happen, depends on the size, shape, and composition of the detector, as well as on the geometric details of the radiation conditions. Typical gamma ray spectroscopy measurements (Fig. 2.6) show the *photopeak* due to the photoelectric effect shifted from the continuum due to Compton scattering events. Over this continuum, two peaks can be found, the *single escape peak* and the *double escape peak*, which correspond to the escaping of one or two annihilation photons of the positron, after a pair production.

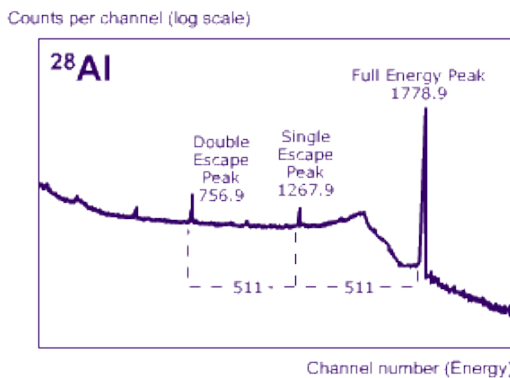


Figure 2.6: Example of gamma ray spectrum of a source of  $^{28}\text{Al}$ . Energy is expressed in keV.

## 2.2 Scintillation detectors

The information of this section comes from the literature [3],[4], [11] and [21]. The content related with scintillation process is summarized here.

The detection of ionizing radiation by the scintillation light produced in certain materials is one of the oldest techniques on record. The scintillation process remains one of the most useful methods available for the detection and spectroscopy of a wide assortment of radiations. When coupled to an amplifying device such as a photomultiplier or a photodiode, these scintillations can be converted into electrical pulses which can then be analyzed and counted electronically to give information concerning the incident radiation.

The primordial contribution to the resolution in this detectors corresponds to the uncertainty in the number of primary produced electrons. This production follows a Poisson statistics, the greater the amount of light of a

given wave length, the greater the amount of primary electrons. More primary electrons implies less relative uncertainty, and therefore, more accurate resolution.

The ideal scintillation material should possess the following properties [4]:

1. It should convert the kinetic energy of charged particles into detectable light with a high scintillation efficiency.
2. This conversion should be linear, the light yield should be proportional to deposited energy over as wide a range as possible.
3. The medium should be transparent to the wavelength of its own emission for good light collection.
4. The decay time of the induced luminescence should be short so that fast signal pulses can be generated.
5. The material should be of good optical quality and subject to manufacture in sizes large enough to be of interest as a practical detector.
6. Its index of refraction should be near that of glass ( $\sim 1.5$ ) to permit efficient coupling of the scintillation light to a photomultiplier tube or other light sensor.

No material simultaneously meets all these criteria, and the choice of a particular scintillator is always a compromise among these and other factors. The most widely applied scintillators include the inorganic alkali halide crystals, and organic-based liquids and plastics. Inorganic scintillators tend to have the best light output and linearity, but with several exceptions are relatively slow in their response time. Organic scintillators are generally faster but yield less light. The intended application also has a major influence on scintillator choice. The high Z-value of the constituents and high density of inorganic crystals favor their choice for gamma-ray spectroscopy, whereas organics are often preferred for beta spectroscopy and fast neutron detection (because of their hydrogen content).

### **2.2.1 Scintillation detector principles**

The basic elements of a scintillation detector consist, generally, of a scintillating material which is optically coupled to a photomultiplier or a photodiode either directly or via a light guide. As radiation passes through the scintillator, it excites the atoms and molecules making up the scintillation

process causing light to be emitted. This light is transmitted to the photomultiplier (or to the photodiode) where it is converted into a weak current of photoelectrons which is then further amplified. The resulting current signal is then analyzed by an electronic system. In general, the scintillator signal is capable of providing a variety of information. Among its most outstanding features are [4]:

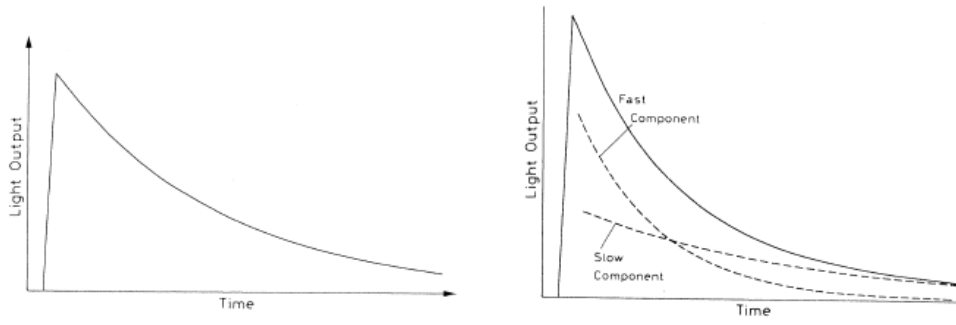
1. *Sensitivity to Energy.* Above a certain minimum energy, most scintillators behave in a near linear fashion with respect to the energy deposited, i.e., the light output of a scintillator is directly proportional to the exciting energy. This makes the scintillator suitable as an energy spectrometer.
2. *Fast Time Response.* Scintillation detectors are fast instruments in the sense that their response and recovery times are short relative to other types of detectors. This faster response allows timing information. This and its fast recovery time allow scintillation detectors to accept higher count rates since the dead time is reduced.
3. *Pulse Shape Discrimination.* With certain scintillators, it is possible to distinguish between different types of particles by analyzing the shape of the emitted light pulses. This is due to the excitation of different fluorescence mechanisms by particles of different ionizing power.

Scintillator materials exhibit a property known as *luminescence*. Luminescent materials, when exposed to certain form of energy, for example, light heat, radiation, etc., absorb and reemit the energy in the form of visible light. If the reemission occurs immediately after absorption or, more precisely within  $10^{-8}$  s, ( $10^{-8}$  s being roughly the time taken for atomic transitions), the process is usually called *fluorescence*. However, if reemission is delayed because the excited state is metastable, the process is called *phosphorescence* or *afterglow*. In such cases, the delay time between absorption and reemission may last anywhere from a few microseconds to hours depending on the material [11].

As a first approximation, the time evolution of the reemission process may be described as a simple exponential decay (Fig. 2.7(a)) [21]

$$N = \frac{N_0}{\tau_d} \exp\left(\frac{-t}{\tau_d}\right) \quad (2.10)$$

where  $N$  is the number of photons emitted at time  $t$ ,  $N_0$  the total number of photons emitted, and  $\tau_d$  the decay constant. The finite rise time from zero



(a) Simple exponential decay of fluorescent radiation. The rise time is usually much faster than the decay time.  
(b) Resolving scintillation light into *fast* and *slow* components. The *solid line* represents the total light decay curve.

*Figure 2.7:* Time evolution of the light reemission process. Picture taken from [3].

to the maximum in most materials is usually much shorter than the decay time and has been taken as zero here for simplicity.

While this simple representation is adequate for most purposes, some, in fact, exhibit a more complex decay. A more accurate description in these cases may be given by a two-component exponential [21]

$$N = A \exp\left(\frac{-t}{\tau_f}\right) + B \exp\left(\frac{-t}{\tau_s}\right) \quad (2.11)$$

where  $\tau_f$  and  $\tau_s$  are the decay constants. For most scintillators, one component is generally much faster than the other so that it has become customary to refer to them as the *fast* and *slow* components (hence the subscripts *f* and *s*). Their relative magnitudes,  $A$  and  $B$ , vary from material to material, although it is the fast component which generally dominates. Figure 2.7(b) shows the relation between these components. As will be seen, the existence of these two components forms the basis for some techniques of pulse shape discrimination.

### 2.2.2 Light output response

The light output of a scintillator refers more specifically to its efficiency for converting ionization energy to photons. This is an extremely important quantity, as it determines the efficiency and resolution of the scintillator. In general the light output is different for different types of particles at the same energy. Moreover, for a given particle type, it does not always vary linearly

with energy. It should be kept in mind that when considering the efficiency of a scintillation detector, the efficiency of the photomultiplier or photodiode must also be taken into account, since they are inseparably coupled.

### Linearity

For many applications it can be considered as a good approximation to assume that scintillators respond in a linear fashion with respect to the exciting energy, which means that the fluorescent emitte light  $L$  is directly proportional to the energy  $\Delta E$  deposited by the ionizing particle,

$$L \propto \Delta E \quad (2.12)$$

Nevertheless, strictly speaking, this linear relation is not true. In reality, the response of scintillators is a complex function of not only energy but the type of particle and its specific ionization [4].

In organic materials, non-linearities are readily observed for electrons at energies below 125 keV, although they are small. For heavier particles the deviations are more pronounced and become very noticeable at lower energies, with the higher ionizing particles showing the larger deviations.

In inorganic materials, the differential light output,  $dL/dx$ , also varies with energy, although the dependence is generally weaker so that deviations are small. Even though for an accurate work this different behavior should be taken into account.

### Pulse Shape Discrimination (PSD)

When materials whose light emission is characterized by two components are considered, both components depend on  $dE/dx$  to some degree. In scintillators where this dependence is strong, the overall decay time of the emitted light pulse will, therefore, vary with the type of exciting radiation. Such scintillators are thus capable of performing *pulse shape discrimination*, i.e., they are able of distinguishing different types of incident particles by the shape of the emitted light pulse. Figure 2.8 illustrates the different decay times, and hence different pulse shapes, exhibited by stilbene when excited by different particles. Similar differences are also observed in other organic materials, particulary liquid scintillators, as well as in inorganic crystals. In CsI(Tl), for example, overall decay times of 0.425  $\mu\text{s}$  for  $\alpha$ -particles, 0.519  $\mu\text{s}$  for protons and 0.695  $\mu\text{s}$  for electrons are found [4].

The explanation for this effect lies in the fact that the fast and slow components arise from the deexcitation of different states of the scintillator. Depending on the specific energy loss of the particle ( $dE/dx$ ), these states are

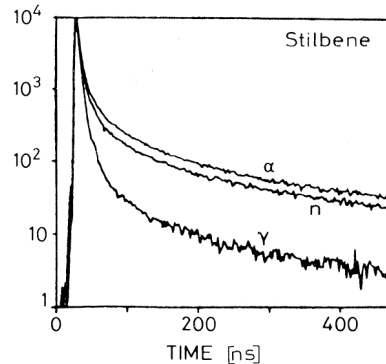


Figure 2.8: Pulse shape of stilbene light for alpha particles, neutrons and gammas rays

populated in different proportions, so that the relative intensities of the two components are different for different  $dE/dx$  [3]. In alkali halides such as CsI, for example, a high ionization loss produces a higher density of free electrons and holes which favors their recombination into loosely bound systems known as *excitons*. These excitons then wander through the crystal lattice until they are captured as a whole by impurity centers, exciting the latter to certain radioactive states (fast component). The singly free electrons and holes, on the other hand, are captured successively resulting in the excitation of certain metastable states (slow component) not accessible to excitons. At low ionization density, exciton formation is less likely and so the proportion of excitons relative to free electrons and holes is lower. The proportion of radiative to metastable excited states will be different, therefore, and hence the pulse shape.

# Chapter 3

## CALIFA

CALIFA (CALOrimeter of In-Flight emitted gAmmas), shown in Fig. 3.1, is a calorimeter that has been proposed as part of the  $R^3B$  detection system for detecting gamma-rays and light charged particles originated in nuclear reactions from relativistic exotic beams.

The  $R^3B$  setup (Fig. 3.2) is a sophisticated experimental setup for the study of nuclear reactions with high-energy radioactive beams, which will be operating in the new international accelerator facility FAIR (Facility of Antiproton and Ion Research) to be built at GSI site in Darmstadt, Germany (Fig. 3.3). The experimental configuration is based on a concept similar to the existing ALADIN-LAND reaction setup at GSI, with substantial improvements in resolution.

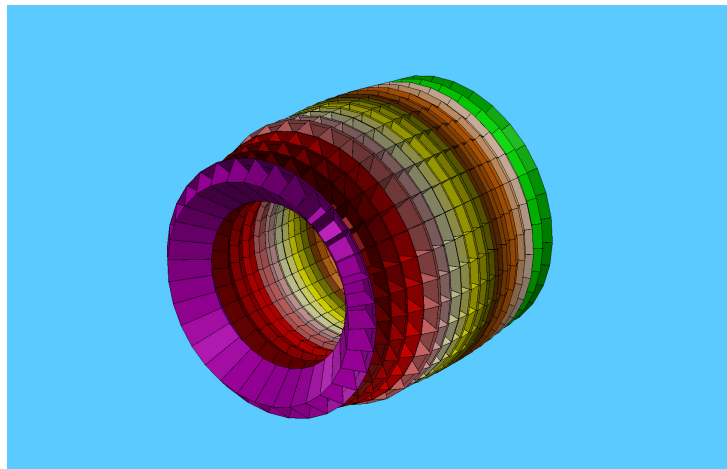


Figure 3.1: Artistic view of the CALIFA detector.

The CALIFA calorimeter will be surrounding the target of the  $R^3B$  experimental setup and will be used in most of the physical cases presented

in the  $R^3B$  technical proposal. This calorimeter will be composed of thousands of inorganic scintillating crystals that serve to detect gammas and light charged particles.

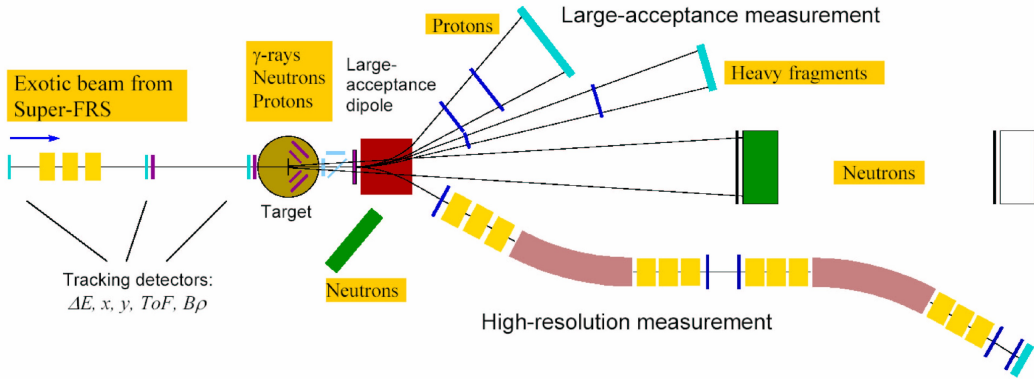


Figure 3.2: Schematic picture of the  $R^3B$  experimental setup

### 3.1 Goals of CALIFA

The most challenging aspect of CALIFA is to ensure its wide dynamic range, from low energy gammas to 300 MeV protons. A typical  $R^3B$  experiment will investigate inverse kinematics reactions induced by projectiles with energies up to 1 GeV/A. This energy introduces a considerable Lorentz boost to gammas emitted in-flight by the reaction remnants. In some cases, accurate  $\gamma$ -ray sum energy is required, while in others the detector must provide  $\gamma$ -ray multiplicities and individual  $\gamma$ -ray energies for spectroscopic purposes.

To overcome the Doppler effect, the angular polar granularity in CALIFA must be kept below  $\sim 1.2$  degrees in some areas, which limits crystal thickness. The detector must also act as a total absorption calorimeter, subtending the angular region from 7 to 130 degrees, to get about 80% geometrical detection efficiency for the emitted gamma distribution. To accomplish this, the device will be composed of a huge number of individual crystals with different shapes and angular apertures for the different polar angle regions.

### 3.2 CsI(Tl) scintillation crystals in CALIFA

Inorganic crystals form a class of scintillating materials with much higher densities than organic plastic scintillators with a variety of different prop-

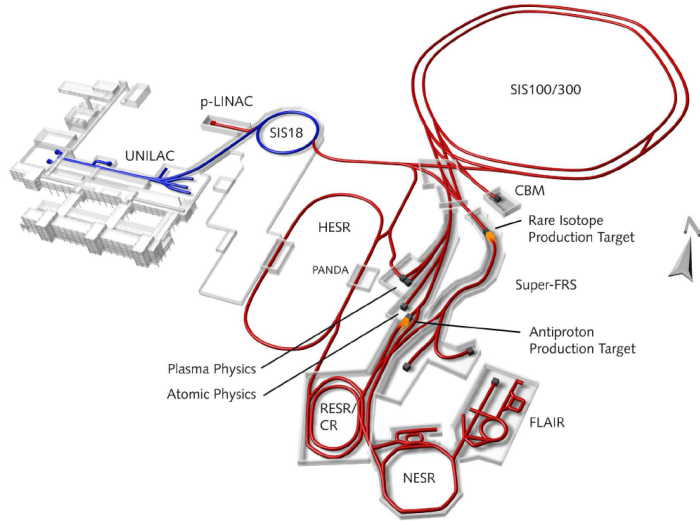


Figure 3.3: The existing GSI facility (blue) and the planned new facility (red)

erties for use as scintillation detectors. Due to their high density and high effective atomic number, can be used in applications where high stopping power or a high conversion efficiency for electrons or photons is required. Many of these crystals have also very high light output, and can therefore provide excellent energy resolution down to very low energies (few hundred keV) [7].

In recent years, CsI(Tl) crystals have been widely used in a large number of experiments. Large CsI(Tl) crystals are relatively cheap to make, easy to handle, and only slightly hygroscopic. Their density is relatively high ( $4.51 \text{ g/cm}^3$ ) and they produce a high light yield ( $\sim 60000 \text{ photons/MeV}$ ). On the other hand, their long scintillation decay time of few  $\mu\text{m}$  requires long integration times at the shaper amplifiers. Moreover, the intrinsic energy resolutions of CsI(Tl) crystals could be as low as 3.8% at 662keV, which establishes a lower limit well suited to their purpose [7].

### 3.2.1 Scintillation mechanism in inorganic crystals with activators

“The scintillation mechanism in inorganic materials depends on the energy states determined by the crystal lattice of the material. Electrons have available only discrete bands of energy in materials classified as insulators or semiconductors. The *valence band* represents those electrons that are es-

sentially bound at lattice sites, and the *conduction band* represents those electrons that have sufficient energy to be free to migrate throughout the crystal. There exists an intermediate band of energies, called the *forbidden band*, in which electrons can never be found in the pure crystal. Absorption of energy can result in the elevation of an electron from the valence band across the gap into the conduction band, leaving a hole in the valence band. In the pure crystal, the return of the electron to the valence band with the emission of a photon is an inefficient process. Furthermore, typical gap widths are such that the resulting photon would be of too high an energy to lie in the visible range.” [4]

“To enhance the probability of visible photon emission during the de-excitation process, small amounts of an impurity, called *activators*, are commonly added to inorganic scintillators. As a result, there will be energy states created within the forbidden gap through which the electron can de-excite back to the valence band (Fig. 3.4). These de-excitation sites are called *luminescence centers* and their energy structure in the host crystalline lattice determines the emission spectrum of the scintillator.” [4]

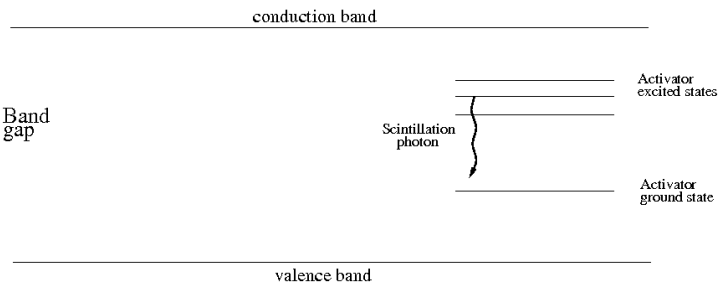


Figure 3.4: Energy band structure of an activated crystalline scintillator.

“A charged particle passing through the detection medium will form a large number of electron-hole pairs. The positive hole will quickly drift to the location of an activator site and ionize it, while the electron is free to migrate through the crystal and will do so until it encounters such an ionized activator. At this point the electron can drop into the activator site, creating a neutral configuration that can have its own set of excited energy states. Its de-excitation will occur very quickly and with high probability for the emission of a corresponding photon in the visible energy range. Typical half-lives for such excited states are of the order of 50-500 ns. Because the migration time for the electron is much shorter, it is the decay time of excited states that therefore determines the time characteristics of the emitted scintillation light”. [4]

There are processes that compete with the one just described. The elec-

tron can create an excited configuration whose transition to the ground state is forbidden. Such states then require an additional increment of energy. One source of this energy is thermal excitation and the resulting slow component of light is called *phosphorescence*. Other possibility exists when occur radiationless transitions between some excited states formed by electron capture and the ground state, in which case no visible photon results. Such processes are called *quenching* and represent loss mechanisms in the conversion of the particle energy to scintillation light [3].

The efficiency  $\eta$  for the conversion of energy deposit in the crystal to scintillation light can be expressed by the relation

$$\eta = \beta \cdot S \cdot Q \quad (3.1)$$

where  $\beta$  is the efficiency of the energy conversion process,  $S$  is the efficiency of energy transfer to the luminescent center, and  $Q$  is the quantum efficiency of the luminescent center. The value of  $\eta$  is the main factor in determining the intrinsic light output of the scintillator [11].

### 3.2.2 CsI(Tl) emission spectrum

The CsI(Tl) gamma-ray excited emission spectrum at room temperature was found to have two primary decay components with decay time constants of  $\tau_1 = 679 \pm 10$  ns (63.7%) and  $\tau_2 = 3.34 \pm 0.14$   $\mu$ s (36.1%), and main emission bands at about 400 and 500 nm. The CsI(Tl) emission spectrum depends on the thallium concentration used as dopant. The shape of this spectrum depends also on the nature of the incident particles producing the scintillation in the crystal (gammas, alphas, betas, protons, etc.). Pulse shape discrimination techniques can therefore be used to differentiate among various types of radiation, particularly clean separations can be achieved between charged particles such as protons or alphas particles on the one hand and electron events on the other hand. This emission spectrum has a significant yield at longer wavelengths (maximum yield at 550 ns) compared to the standard NaI(Tl) scintillation crystals. Since its spectral response covers this wavelength region, this crystal is ideal for coupling with silicon photodiodes [13].



# Chapter 4

## Experimental Setup

This chapter describes the setup used to perform the test on the *ProtoZero* prototype of CALIFA. This test took place at the facility of the GSI Helmholtzzentrum für Schwerionenforschung at Darmstadt (Germany). The ProtoZero prototype was part of a set of detectors installed in Cave C, to study the reactions produced when a pulsed  $^{197}\text{Au}^{65+}$  beam of  $E = 400 \text{ AMeV}$  impinge on a Pb target. The goals were to test the energy resolution of the crystals, particle identification algorithms and the new data acquisition system, based on a new FPGA able to perform real-time data analysis.

### 4.1 ProtoZero, first step towards CALIFA

The GENP (Grupo Experimental de Núcleos y Partículas) at the University of Santiago de Compostela participates in the design and development of the CALIFA calorimeter. A prototype of this calorimeter called *ProtoZero*, formed by fifteen bi-frustum-shaped CsI(Tl) scintilling crystals (Fig. 4.1) coupled to avalanche photodiodes contained inside an aluminum box for electric and external light isolation (Fig. 4.2), has been built. This prototype is created to check different types and brands of components, including crystals, with different sizes and shapes, crystal wrappings, adhesives resins, and electronic performances. Different tests were carried out, under high energy gamma beams at NEPTUN in TU Darmstadt and at CMAM in Madrid, and under proton beam in the facilities of Uppsala, Sweden.

### 4.2 General features

The CALIFA prototype detector was part of a larger experimental set-up used as a preparation for an ASY-EOS experimental campaign. The

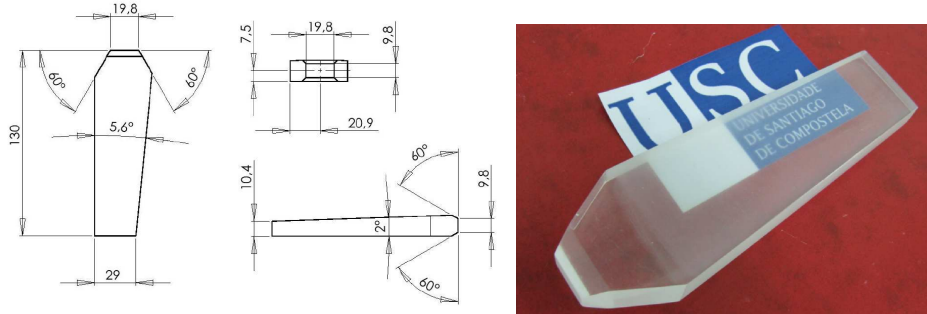


*Figure 4.1:* Design of bi-frustum-shaped crystal. All dimensions are in mm.

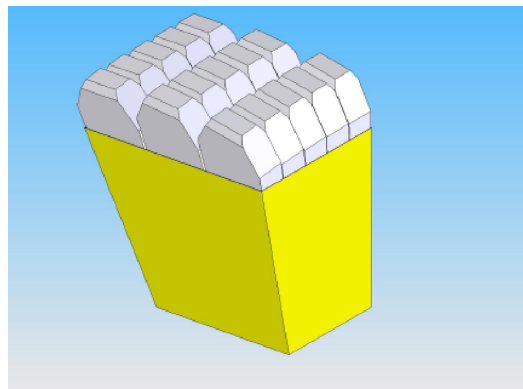


*Figure 4.2:* ProtoZero design.

ProtoZero was located at an azimuthal angle of about  $45^\circ$  from the beamline with a distance of about 1.50 m from the target (Fig. 4.3). A fast

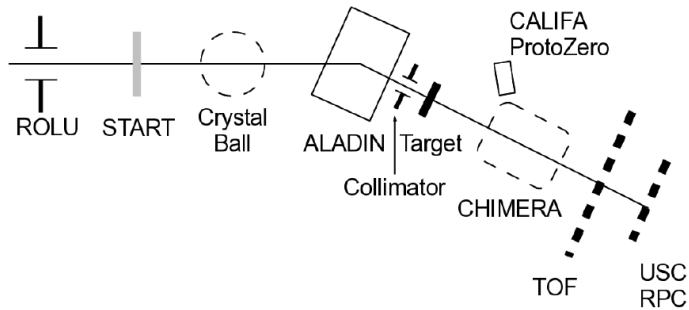


*Figure 4.3:* Experimental setup of the experiment including the CALIFA ProtoZero setup.

scintillator plastic was mounted right in front of the detector box (as seen from the target). In addition, the signal of a start detector mounted in front of the magnet, was recorded.

The nine 13 cm long CsI(Tl) crystals, (referred to as *short crystals*), arranged in a 3x3 array and, on top of them, four 18 cm long ones (*long crystals*) arranged in a 2x2 array were mounted inside a box (Fig. 4.4). The short crystals were wrapped inside one layer of teflon tape, one 3M VM2000 radiant mirror film<sup>1</sup> and finally another layer of teflon tape. The long crystals were wrapped inside one layer of 3M VM2000 and mounted within a carbon fiber case.

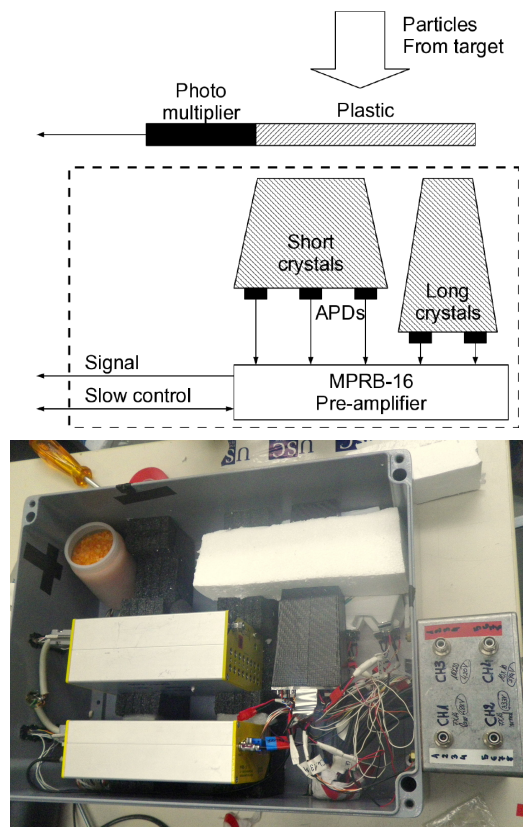


Figure 4.4: Scheme and picture of the detector box hosting the crystals with their APDs and Mesytec MPRB-16 pre-amplifier

Hamamatsu Large Area APDs (LAAPD) as well as double APDs were

<sup>1</sup>This material is a multi-layered polymeric film. The outside layer is polyethylene. It reflects more than 98% of the visible light, it is metal free, therefore non-corrosive and non-conducting.

attached to the crystals within their wrapping. Since the collected charge in the detector is so small that it is impractical to deal with it directly, preamplifiers provide a first and fast amplification of the detector's response to incident particles. A Mesytec MPRB-16 multi-channel pre-amplifier (Fig.4.5) was installed inside the box. This preamplifier is charge-sensitive, which means that it provides an output pulse whose amplitude is proportional to the total integrated charge in the pulse provided to its input terminals.



*Figure 4.5:* Mesytec MPRB-16 pre-amplifier front panel

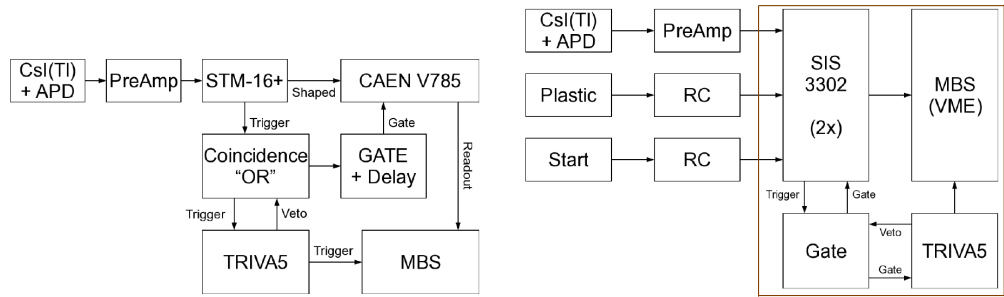
After preamplification, there is an amplification stage that provides an increase of the amplitude and some signal shaping. Amplification is needed since the output signal of the preamplifier is in the range of millivolts and cannot travel very far, or be manipulated without losing information or even being lost in the noise. Shaping is both useful and necessary because it prevents pile-up of pulses (making pulses short enough so that the whole system may be ready for the next pulse as soon as one pulse is detected), and improves the signal-to-noise ratio. The amplifier used in this test was a Mesytec STM-16+, a 16-channel spectroscopy amplifier.

Finally, signals were digitized through three different data acquisition systems (DAQ): a conventional, analog to digital converter ADC, a fully digital readout using a fast sampling ADC to store signal traces for off-line analysis, and a second fully digital readout using a flash ADC connected to a FPGA (Field Programmable Gate Array) for real-time data analysis.

### 4.3 Different readout systems

For the analog setup, shown in figure 4.6(a), the preamplifier's signal was led into the Mesytec STM-16+ all-in-one NIM module, a spectroscopy am-

plifier which includes a multi-channel shaper, timing filter and other (not used) features. Its discriminated output was vetoed by the TRIVA5 dead-time output. TRIVA5 is a trigger module dedicated to guarantee a correct inhibition of ADC gates and TDC starts during conversion and read-out time as well as the collection of corresponding subevents to the complete event. The resulting signal was used to trigger the *Multi Branch System* (MBS), the acquisition software, readout procedure via the TRIVA5 module, and to generate a gate for the peaksensing ADC CAEN V785, a module housing 32 Peak Sensing Analog-to-Digital Conversion channels. Each channel is able to detect and convert the peak value of the positive analog signals (with  $>50$  ns risetime) fed to the relevant connectors. As this setup doesn't allow PID, it was mostly used as a test and a backup.



(a) Experimental setup for analog readout. (b) Experimental setup for the SIS3302 readout.

Figure 4.6: Data acquisition system setup

During the same experiment, another setup was used (fig. 4.6(b)). In this setup, two SIS3302 multichannel fast sampling ADCs (Fig. 4.7) were used to record full event traces as well as their determined energies in order to be analyzed later. The SIS3302 is an eight channel ADC/digitizer board with a sampling rate of up to 100 MHz (for each individual channel) and a resolution of 16-bit. The board is a single width 6U VME card, which has no special voltage requirements. The flexible combination of DDR2 memory technology data storage in combination with FPGA based data handling/movement allows for a generic design which covers a variety of applications [19].

The actual readout was controlled by MBS. The preamplifier's outputs were connected to the ADCs' inputs using a differential to single ended converter box. In each channel, the sampled signal is processed using a FIR-filter and compared to a given threshold. As soon as the signal exceeds the threshold, a logic pulse is generated. While the system is busy reading out the data, all the new events' triggers should be discarded. Therefore, the ORed pulse

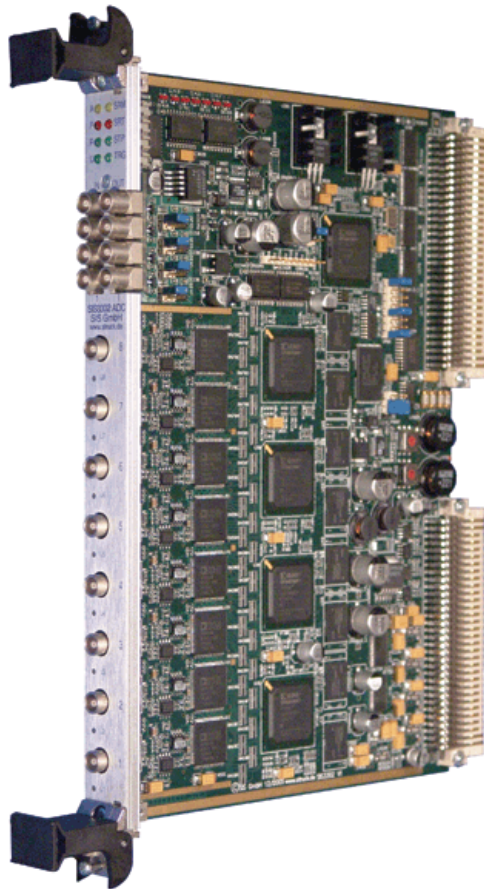


*Figure 4.7: SIS3302 Sampling ADC.*

is inhibited by means of the deadtime output of the TRIVA5 trigger module. Additionally to triggering the readout via TRIVA5, the vetoed signal is used to trigger the readout of all the channels of both the SIS3302 modules. In addition, the plastic scintillator's and the start detector's RC-filtered signals were recorded to discriminate between background and particles actually originating from the target.

#### 4.4 Avalanche photodiode

Photodiodes (PDs) were the photodetectors chosen as the best option for the CALIFA purposes. Photodiodes are made of a thin silicon layer which, upon illumination, creates free-charge carriers (holes and electrons). After optically coupling the photodiodes with the crystals, the light pulse produced

in the scintillator is collected in the photodiode and each individual photon has a probability of exciting an electron, generating a positively charged electron hole. It creates a very small charge pulse that can be amplified with a charge preamplifier.

Compared to commonly used photomultipliers, photodiodes offer the advantages of a higher quantum efficiency (70% between 500 nm and 900 nm) [13] and hence, a better energy resolution. Photodiodes offer lower power consumption, more compact size, and most important of all, are almost insensitive to magnetic fields. The best resolution obtained with avalanche photodiodes coupled to CsI(Tl) crystals are around 4,5% [13], being this one of the main reasons for choosing Avalanche PhotoDiodes or APDs (Fig. 4.8) as the ideal photosensors for the CALIFA Barrel scintillation crystals.

APDs incorporate an internal gain increasing the collected number of charge carries by an *avalanche process*. Charge carriers are accelerated sufficiently between collisions to create additional electron-hole pairs along the collection path. This acceleration is obtained by applying a voltage to the APD, but, since the gain factor is extremely sensitive to the applied voltage, avalanche photodiodes require well-regulated high-voltage supplies.

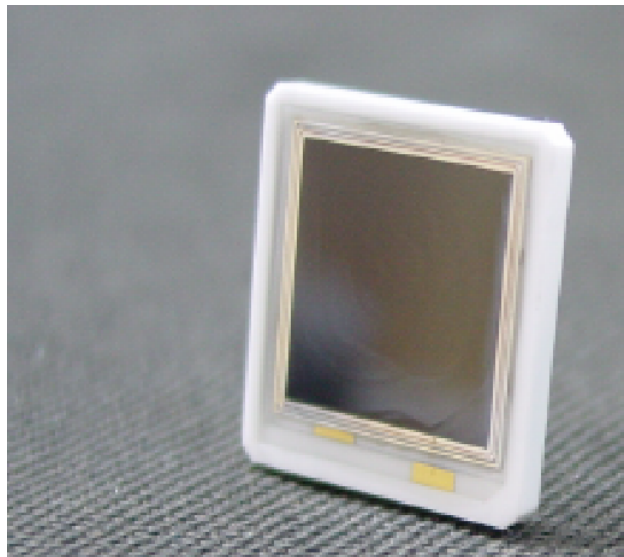


Figure 4.8: APD, Avalanche PhotoDiode

The APDs used in the *ProtoZero* were S8664-1010 from Hamamatsu Photonics K.K. which has the parameters shown in the table 4.1.

Model	S8664-1010
Dark current $I_D^e$	10 - 31 nA
Break-down voltage $V_{brk}^f$	455 - 670 V
Bias Voltage $V_G^{e,f}$	400 - 420 V
Capacitance $C_{det}^f$	270 pF

<sup>e</sup>Measured at a gain of 50.

<sup>f</sup>Measured at 25°C.

Table 4.1: Hamamatsu APD parameters.

# Chapter 5

## Data Analysis

In this chapter I will explain the analysis done over the data acquired with the setup shown in the previous chapter. The two main goals of this analysis are to study and improve the capabilities of particle identification and the energy resolution. Different methods and algorithms are going to be tested to extract the maximal amount of information from the existing data.

### 5.1 Binomial smoothing filter

Our data from the fastADC SIS3302 are disturbed by periodic high-frequency noise as we can see in Fig. 5.1, so it becomes necessary to use a smoothing filter to remove that noise and improve the signal-to-noise ratio. I have used a binomial smoothing filter which is appropriate for this kind of noise and it performs as follows [25]: let  $\{x_n\}$  denote the fastADC sample sequence which is going to be filtered. The filter computation is performed by a moving-average smoothing of the data sequence, controlled by a set of coefficients  $b_k$ . The filtered output data sequence  $\{y_n\}$  is given by

$$y_n = \sum_{k=-N_p}^{N_p} b_k X_{n-k} \quad (5.1)$$

where the  $(2N_p+1)$ -points smoothing sequence  $b_k$  is defined by normalized binomial coefficients

$$b_k = \binom{2N_p}{N_p + k} / 4^{N_p} \quad (5.2)$$

where  $N_p > 0$  is the filter order which must be chosen in order to obtain a desired upper cutoff half-transmission frequency  $f_{0.5}$  as follows

$$f_{0.5} = 0.5 f_s (2/\pi) \arccos(0.5^{1/2N_p}) \quad (5.3)$$

where  $f_s$  is the fADC sampling frequency.

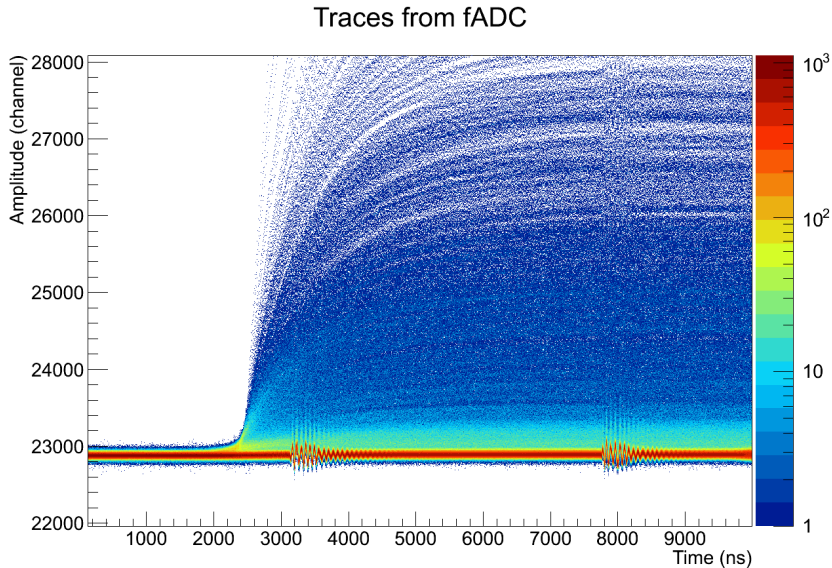


*Figure 5.1:* Traces from the fastADC. It is possible to see high-frequency noise at different points (between 3100 and 4500 ns and between 7750 and 9000 ns) which must be suppressed by a smoothing filter.

A compromising situation was taken between a good signal-to-noise ratio and a not shaping information lost to find a good value for  $f_{0.5}$ . The filter order chosen was  $N_p = 150$ , which with the SIS3302 sampling frequency  $f_s = 100MHz$  give us  $f_{0.5} = 2.16MHz$ . The result of this smoothing filter over our traces is shown in Fig. 5.2.

## 5.2 Moving Window Deconvolution

As it was shown in the previous chapter, the basic elements of our system are an APD detector connected to a charge sensitive preamplifier and a shaping amplifier. Any radiation event produces an amount of charge proportional to the absorbed energy. That charge results in a steplike waveform at the preamplifier output. The preamplifier output signal  $U_p(t)$  is described by

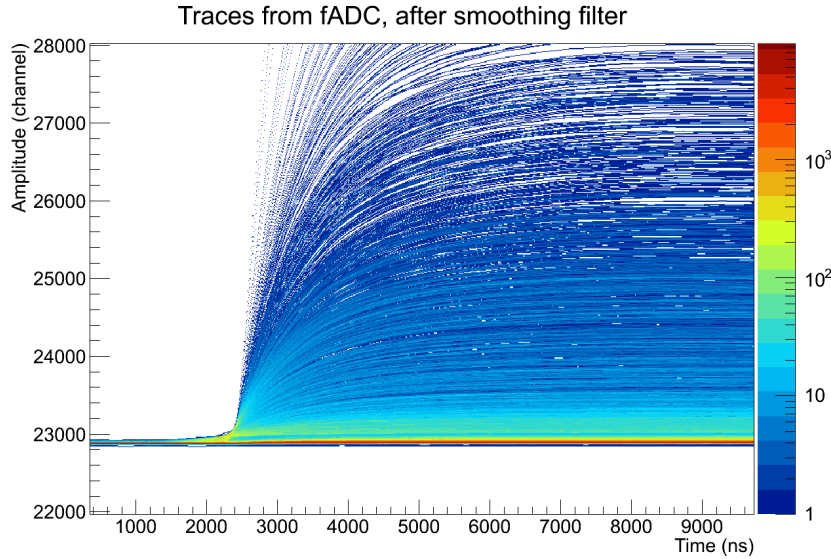


*Figure 5.2:* Traces from the fastADC after the binomial moving-average smoothing algorithm treatment, with an upper cutoff half-transmission frequency of  $f_{0.5} = 2.16\text{MHz}$

a convolution between the charge distribution function  $g(t)$  and the preamplifier impulse response  $f(t)$  [28]

$$U_p(t) = \int_{-\infty}^{+\infty} g(\tau) f(t - \tau) d\tau \quad (5.4)$$

After a first step of quantization of the preamplifier signal by a fast Analog-to-Digital Converter (fastADC), the convolution integral becomes a convolution sum, which can be simplified taking into account that the analog part of the system is causal, the output depends only on the present and past values of the input

$$U_p(i) = \sum_{j=z}^i g(j) f(i - j) \quad \text{for } i > z \quad (5.5)$$

where  $z$  is an arbitrary time reference.

Furthermore the charge function is right-side limited (the charge distribution under normal conditions is time limited). Assuming that there are no charges associated with a single event outside of the observation interval, or window, with a length of  $L$ , then the total charge in the window is obtained

as

$$G(n) = \sum_{i=n-L}^n g(i) \quad \text{for } n = z + L \quad (5.6)$$

Assuming that the impulse response of the analog part is known, the set of equations (5.5) can be solved for the charge matrix  $\{g\}_{(z,z+L)}$ [24]

If we increase  $z$  one by one we can obtain a continuous sequence of  $G(n)$  results, each one representing the total charge released in its associated window, where each window is shifted against the previous one by one sampling interval. This process is called Moving Window Deconvolution. A scheme of its operation is shown in Fig. 5.3.

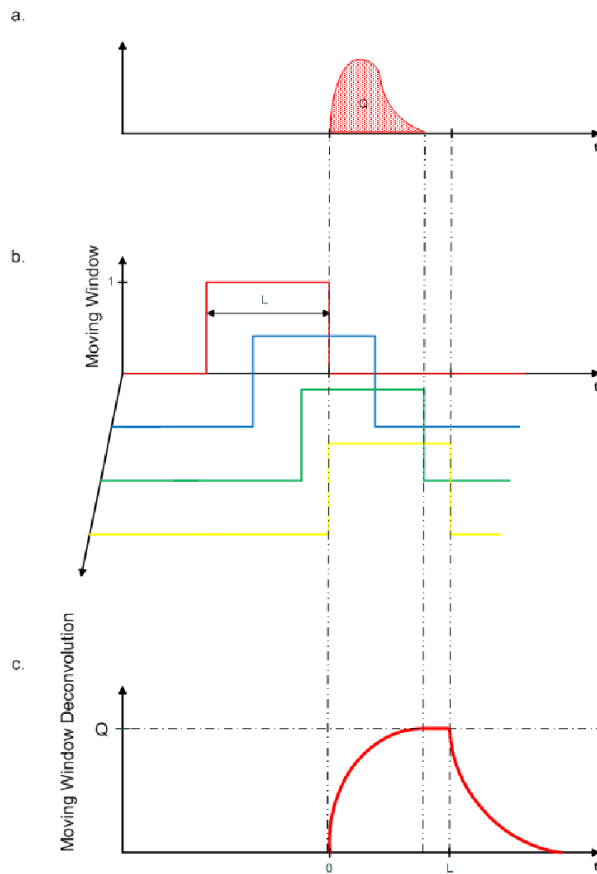


*Figure 5.3:* Qualitative scheme of the MWD operation over a typical signal. The MWD value at a distance  $L$  from the beginning of the signal corresponds with the integrated charge  $Q$ .

In our case, we can represent the impulse response of our preamplifier as a

exponential decay, such as in the most common cases of systems with resistor discharged preamplifiers[24],  $f(n) = e^{-\frac{n}{\tau_p}}$ , where  $\tau_p$  is the characteristic decay time of the preamplifier.

Applying  $f(n)$  to the last equation we obtain a simple recursive equation for the total charge  $G(n)$  in a window L

$$G(n) = U_p(n) - U_p(n-L) + (1 - e^{-\frac{1}{\tau_p}}) \sum_{j=n-L}^{n-1} U_p(j) \quad \text{for } n > z+L \quad (5.7)$$

equation which is analytically developed in Appendix A.

Using this method we are able to separate the preamplifier contribution from the charge distribution function, being its integral proportional to the output of the method. Furthermore, this method gives us a ballistic deficit correction [26] improving our energy resolution.

In order to check the characteristic decay time of my preamplifier ( $\tau_p$ ) I have analyzed signals of cosmic rays obtained with the same crystal, APD and preamplifier and readout with an oscilloscope. This way, it is possible to see the signal output of the preamplifier. The signals amplitude and rise time depend to a great extend on the particle type and energy, but the decay time of the preamplifier is expected to be much larger than any other response time in this setup, making possible to use cosmic rays as a generic signal for the calculation of this decay time.

It would be preferable to accumulate the complete signal but it was not possible, as we can see in Fig. 5.4 the adquisition is limited to 100  $\mu s$  as a compromising situation because these data were used for different purposes.

The contribution of any particle can be assumed practically negligible 30  $\mu s$  after the takeoff of the signal. Fitting the signal to a exponential function after this point we find the characteristic decay time of the preamplifier to be  $\tau_p = 133 \mu s$ . This value confirms that the decay time is high enough to disentangle the charge deposition from the preamplifier effects.

### 5.3 Baseline subtraction

The zero value of amplitude in a fastADC is not fixed. The capability of moving the offset of one fastADC is useful for registering signals as small as desired. This shift of the offset produces a *baseline* which corresponds to zero amplitude events.

As explained in Appendix A, it is mandatory to subtract the baseline for applying the MWD. From one event to the next the baseline can be different even with similar signals, making the accuracy of our results decrease.

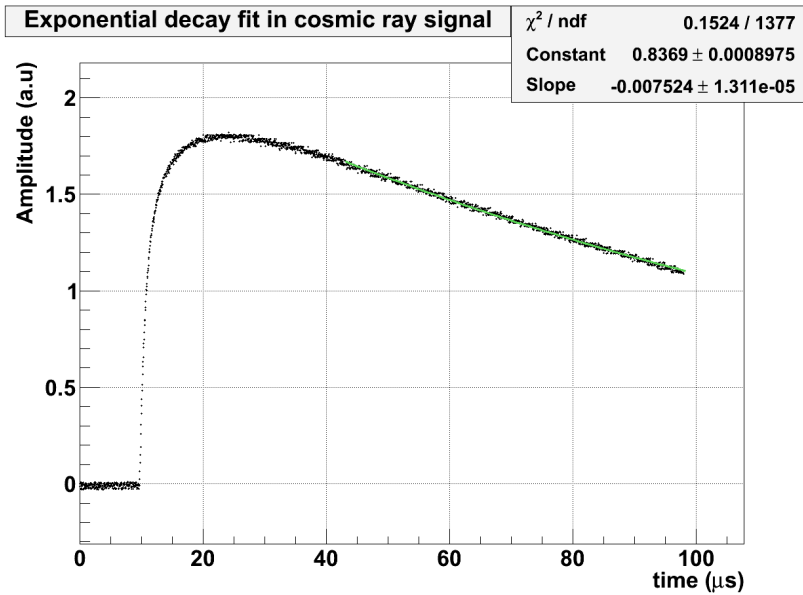


Figure 5.4: Exponential decay fit in the last part of a signal produced by a cosmic ray read after the preamplifier.

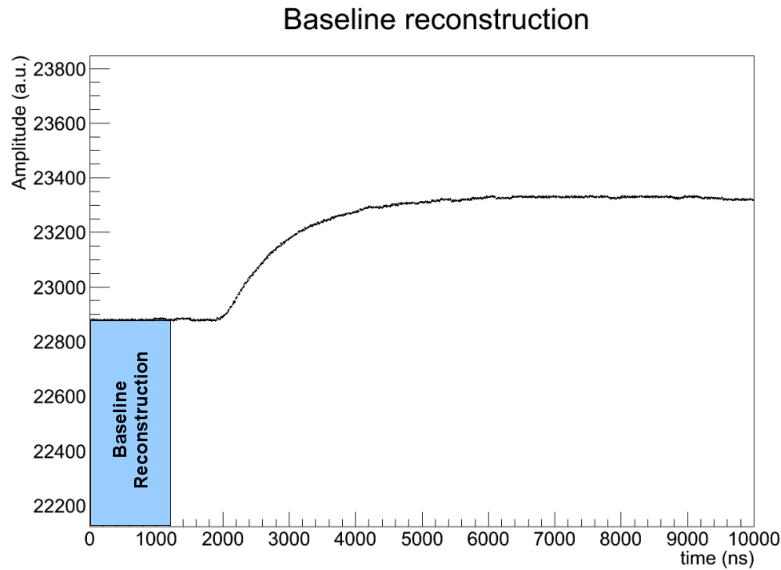


Figure 5.5: Baseline reconstruction as an average of amplitude values in the range of the first 1000 ns.

The method that I used for determining the baseline consists on calcu-

lating the average value of the signal amplitude in the first flat part of each trace along a range wide enough to have a well precise result but not too large to include signal contributions. The range was limited to the first 1200 ns. This baseline was systematically removed from each point of the trace and recalculated for each event.

## 5.4 Energy Calibration

One of the goals of any calorimeter is measuring the energy of each particle going through. For this reason, the energy calibration is one of the main steps in the analysis of a calorimeter. The energy calibration provides a unique relationship between a characteristic parameter of the signal, typically the integrated charge, and the deposited energy inside the crystal.

Gamma sources with peaks whose energies are well known are used for calibration purposes. In our case, the energy calibration was carried out with a  $^{60}Co$  source. This nucleus decays by emitting  $\beta^-$  particles going to two different excited states of  $^{60}Ni$  with different probabilities. Afterwards, these excited states decay emitting two well energy defined photons, as we can see in Fig. 5.6, one with an energy of 1.1732 MeV and another of 1.3325 MeV.

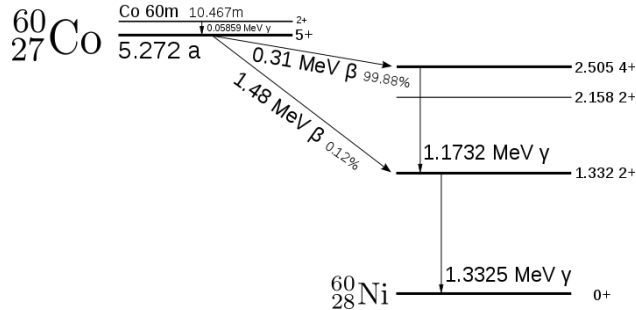


Figure 5.6: Energy levels of  $^{60}Co$  decay.

The integrated charge of a signal is closely related to the released energy by the particle producing that signal. The optimal parameter to determine the energy of the incident particle will be the maximum value of the trace after a Moving Window Deconvolution (MWD) procedure, which corresponds with the integrated charge. The traces of the signals produced by a  $^{60}Co$  source in our detectors are shown in Fig. 5.7. After removing the preamplifier decay contribution by applying a MWD, both photopeaks are clearly distinguishable.

The position of both peaks is obtained by fitting the MWD amplitude histogram with a Gaussian fit for each peak over a quadratic background

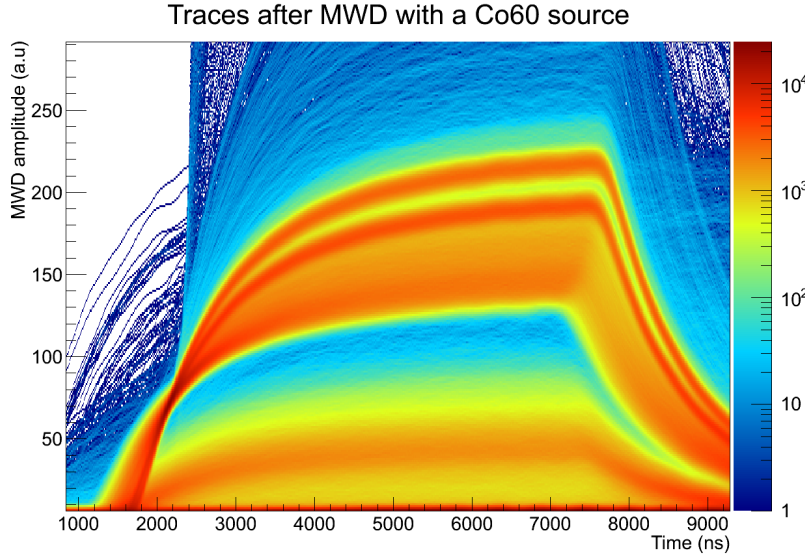


Figure 5.7: Traces from  $^{60}Co$  source after MWD. Both peaks are observable.

which agrees with the experimental data (Fig. 5.8).

The idea of using Gaussian fits comes from the assumption that the formation of each charge carrier is a Poisson process. If an average total number  $N$  of charge carries is generated, one would expect a standard deviation of  $\sqrt{N}$  to characterize the inherent statistical fluctuations in that quantity. In a real situation there are many variations event by event due to particularities in the different stages (emission, transmission and conversion). All of them produce small random effects, which converge back to a Gaussian distribution. The response function should have a Gaussian shape as we see experimentally.

The value of the mean of each peak resulting from this fit is  $\mu_1 = 191.4$  for the lower energy peak and  $\mu_2 = 216.8$  for the higher energy one. The energy calibration equation comes from the linear relation between these mean values and the energy assigned to the peaks in the literature [11] resulting in the relation

$$E(MeV) = -0.0272 + 0.00627 * Q \quad (5.8)$$

Once the energy calibration is done, besides being able to determine the energy of the particles hitting the crystal, it is possible to calculate the crystal energy resolution. This can be done fitting a double gaussian fit plus quadratic background as before, but now after calibration.

The usual way to present the energy resolution of a peak is through the ratio between the Full Width at Half Maximum (FWHM) and the mean of

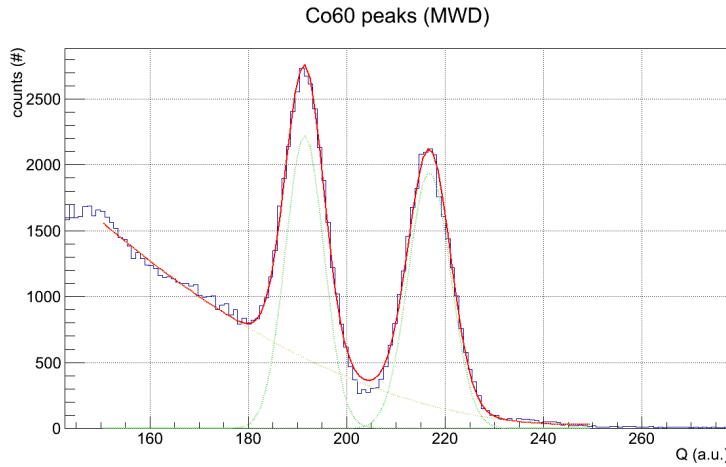


Figure 5.8: Integrated charge with a  $^{60}Co$  source through MWD. Double gaussian fit and quadratic background.

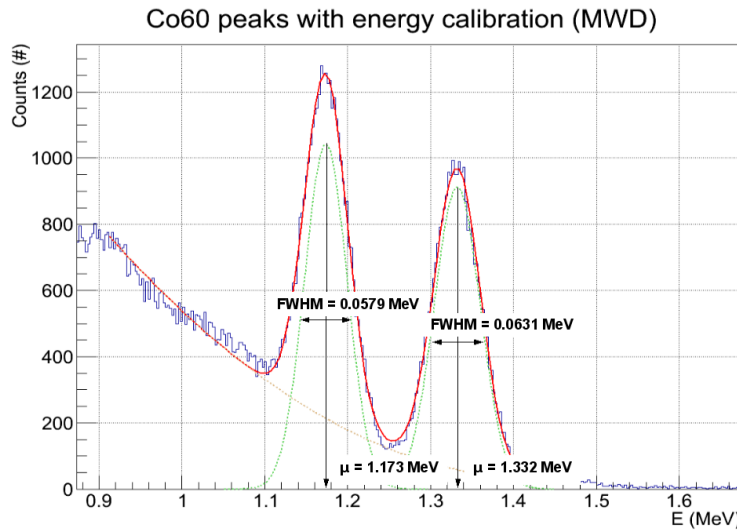


Figure 5.9: Energy resolution of crystals in photopeaks of a  $^{60}Co$  source.

the peak, in percentage. In a Gaussian distribution there is a relationship between standard deviation  $\sigma$  and the FWHM. We find the half-maximum points  $x_0$  as follows

$$e^{-(x_0 - \mu)^2 / 2\sigma^2} = \frac{1}{2} \quad (5.9)$$

and solving,

$$x_0 = \pm\sigma\sqrt{2\ln 2} + \mu \quad (5.10)$$

The full width at half maximum is therefore given by

$$FWHM = x_{0+} - x_{0-} = 2\sqrt{2\ln 2}\sigma \quad (5.11)$$

From the Gaussian fits, we obtain the following values for the standard deviation:  $\sigma = (2.46 \pm 0.02) \cdot 10^{-2}$  MeV and  $\sigma = (2.68 \pm 0.02) \cdot 10^{-2}$  MeV. The corresponding FWHM values are shown in Fig. 5.9. Through this method we find a resolution of  $(4.94 \pm 0.05)\%$  for the 1.173 MeV peak and a resolution of  $(4.74 \pm 0.04)\%$  for the 1.332 MeV peak. These results show an improvement of  $\sim 1\%$  for the first peak and  $\sim 0.6\%$  for the second one respect to the last analysis with the same shape crystals [12].

For gamma energy measurement purposes, another different method was developed and implemented by hardware in our VME Digitizer SIS3302. This method consists of a FIR filter. Two ranges are defined with a width (P). They are shifted one respect to the other in a distance (sumG). The signal values are integrated inside of each range, and the resulting value of the differentiation of both ranges is the output of the FIR filter.

$$FIR\ filter\ value = SUM2 - SUM1 + offset \quad (5.12)$$

where

$$SUM1 = \sum_{i=x}^{x+P} Si \quad (5.13)$$

$$SUM2 = \sum_{j=x+sumG}^{x+P+sumG} Sj \quad (5.14)$$

A schematic example is shown in Fig. 5.10. The parameters summing the range width (P) and the distance between integrals (sumG) are modifiable by the user.

As a result of this method, we find trapezoidal shape signals (Fig. 5.11) whose maximum amplitude can be used as an energy observable.

Proceeding the same way as explained before with respect to the energy calibration and resolution, I have obtained a very good resolution, even better than the resolution obtained using the MWD method. With standard deviations shown in Fig. 5.12 the resolution values are  $(4.70 \pm 0.04)\%$  for the lower energy peak and  $(4.52 \pm 0.04)\%$  for the higher energy peak, results which, taken into account that the FIR filter is already implemented in SIS3302, confirms that the VME digitizer SIS3302 is ideal for gamma spectroscopy purposes.

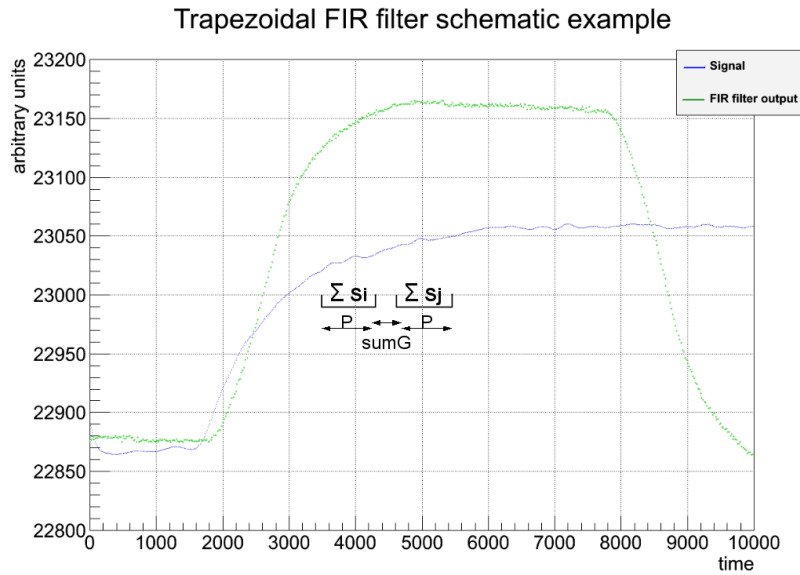


Figure 5.10: FIR filter schematic example.

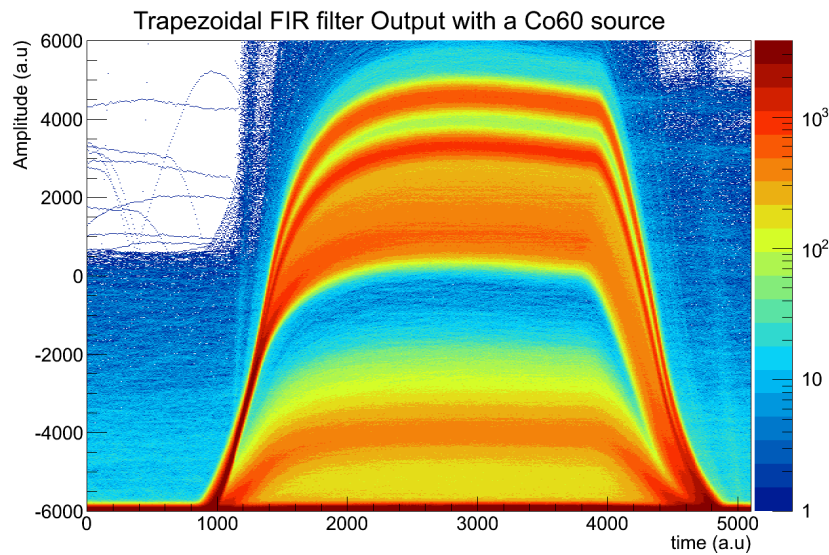
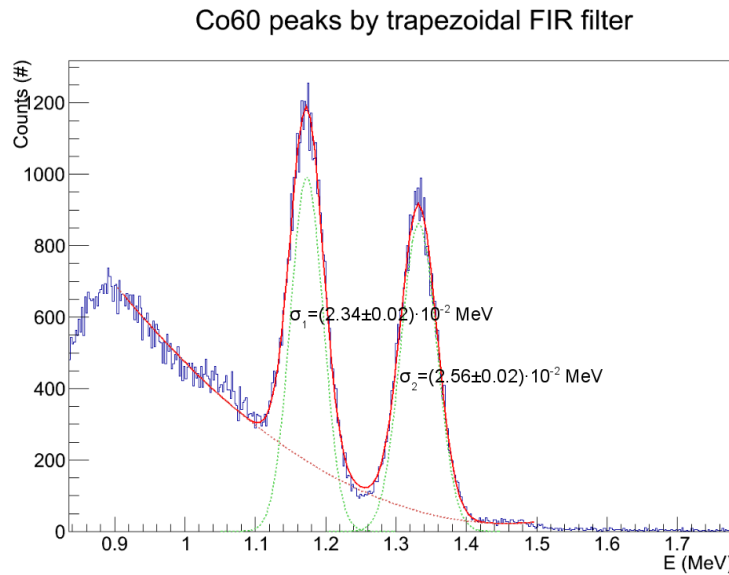


Figure 5.11: Trapezoidal shape signal of the FIR filter.

## 5.5 Pulse Shape Analysis for PID

Another important goal of any calorimeter, besides measuring particle energy, is having the capability of identify particles. Many different studies



*Figure 5.12:*  $^{60}\text{Co}$  photopeaks. Double Gaussian fit for maximum amplitude of FIR filter. With this method we obtain the best resolution, 4.70% for the lower energy peak and 4.52% for the higher energy peak.

were carried out looking for any correlation between pulse shape and the nature of particle which creates the pulse. The ongoing analysis has the same purpose. I will inspect different properties of the pulses to find any connection with the incoming particle.

### 5.5.1 Signal Rise Time

As the Bethe formula says, the energy deposited per length unit by a charged particle going through a material is proportional to the square of its atomic number  $Z$ . The higher the atomic number is, the larger the energy loss per length unit, and at the same time, the faster the rising of the signal.

A schematic example of signal shapes produced by a photodiode coupled to a CsI scintillation crystal for different particles is shown in Fig. 5.13, where the particular situation in which photons reach directly the photodiode triggering a very fast signal is included.

Furthermore, if we compare the rise time with the amplitude of signals for a given particle we will find a clear relationship, the larger the amplitude, the longer the rise time. This is because a higher amplitude means higher energy, and again according to the Bethe formula, the energy loss of a charge particle

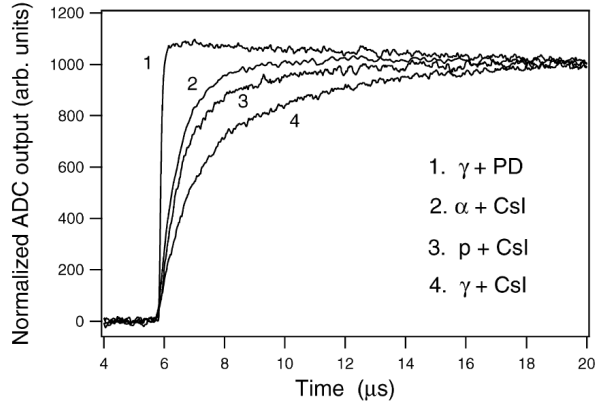


*Figure 5.13:* Schematic signal shapes with different particles hitting the scintillation crystal. The case when photons arrive directly to the photodiode is included (1).

has an inverse dependence with the velocity, making the energy loss slower for fast energetic particles. This last relationship is kept until particles have enough energy to cross the whole crystal (*Punch-through*), escaping with part of the energy. When this effect happens, the signal amplitude does not correspond to the particle's energy, and crystals are not sensitive to the most significant part of energy loss curve, which corresponds to the final part of the track (the Bragg peak). Without this peak, the rest of the curve is practically flat, which means that the rise time will be practically the same, independently of the energy of the particle.

An example of this situation is shown in Fig. 5.14. In this figure we can see that the risetime increases with the energy loss in the detector. Each particle defines a different relationship between both observables, in the lower part of the plot we find the three hydrogens (proton, deuterium and tritium), just above them the two heliums, and in the upper part the heavier particles. All these curves reach a point where the proportional behaviour is lost. At this point, the particles suffer punch-through, they are not stopped in the crystal, and the correlation between energy loss and risetime disappears. Electrons and gammas are seen in a different place because of their different interaction with matter. The labels *LE* and *HE* refer to Low and High energy.

In the case of photons, the way they interact with matter is completely different from that of charged particles, and they are expected to produce a signal with a rise time slower than in the case of charged particles.

As a method for determining the rise time of the signals, I have evaluated

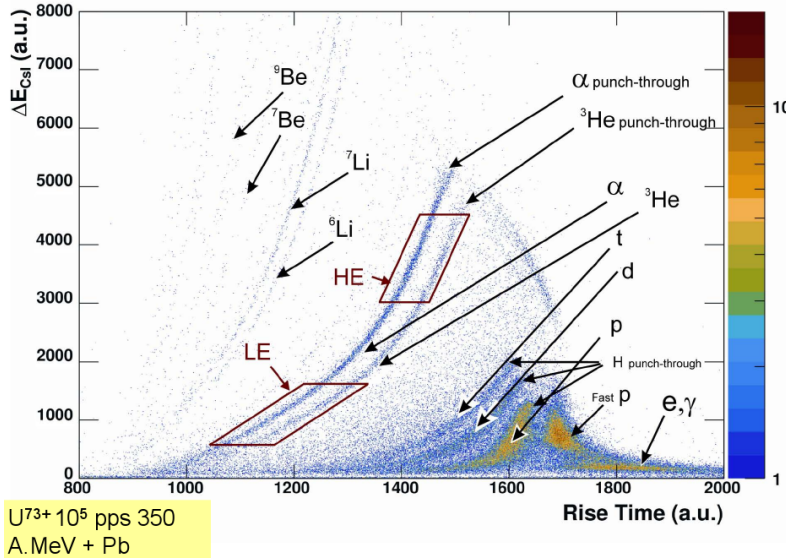


Figure 5.14: Energy lost in CsI crystals versus rise time of the signal. Picture taken from [31].

the time between 20 and 80 per cent of the total signal amplitude. In order to do that, first it is necessary to divide the trace in small steps and fit each one to a third order polynomial, forcing the resulting trace pieces to be continuous. I have divided each trace in 100 steps of 10 ADC sampling times each (Fig. 5.15).

As a result of this method, I will show in figure 5.16 a plot of the rise time versus the amplitude for gammas from a  $^{60}\text{Co}$  source. In figure 5.17, the same plot for particles coming from the reaction is shown.

The analysis of these results will be a topic of discussion in the next chapter.

### 5.5.2 Fast & Slow Components

As it was already mentioned in Chapter 2, it is widely used a two-component exponential function to parametrize the output light produced in a CsI(Tl) crystal

$$L(t) = N_f e^{-\frac{t}{\tau_f}} + N_s e^{-\frac{t}{\tau_s}} \quad (5.15)$$

where  $N_f e^{-\frac{t}{\tau_f}}$  is *the fast component*, with  $\tau_f = 679$  ns, and  $N_s e^{-\frac{t}{\tau_s}}$  is *the slow component*, with  $\tau_s = 3.34$   $\mu\text{s}$ .

The information contained in each component of the light output could be used for identification purposes: the fast component ( $N_f$ ) is related to how

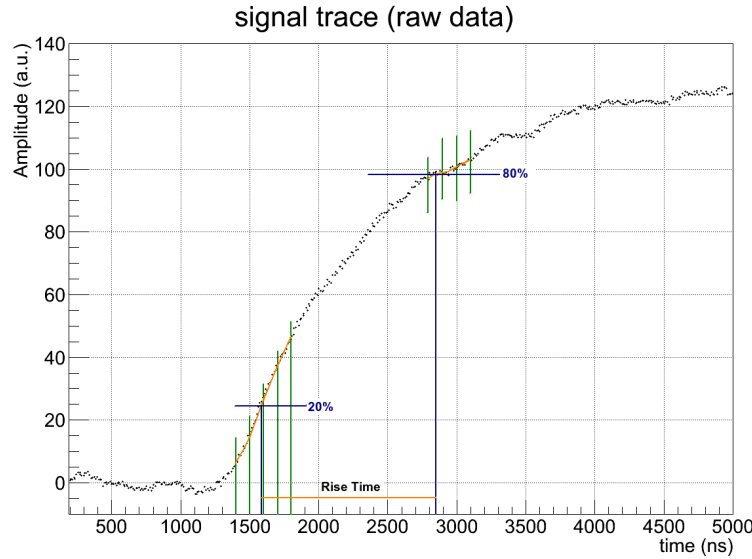


Figure 5.15: Rise time calculation, time between 20% and 80% of signal amplitude.

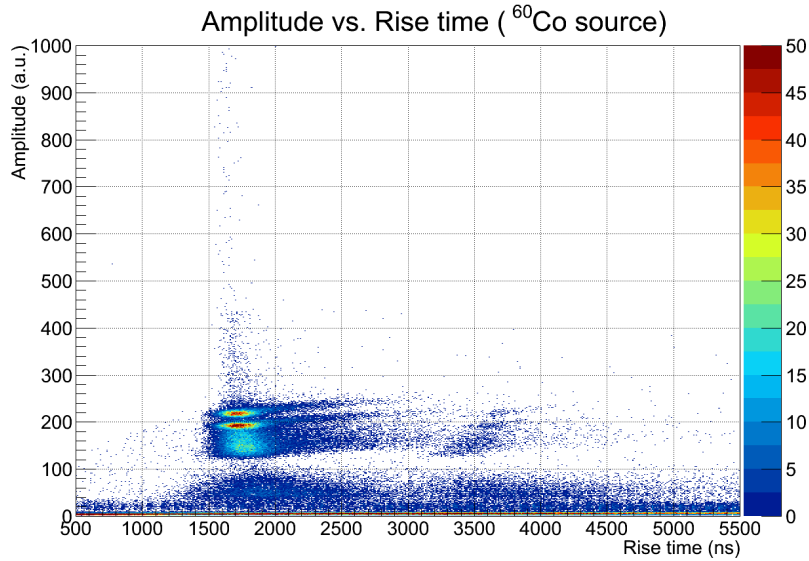
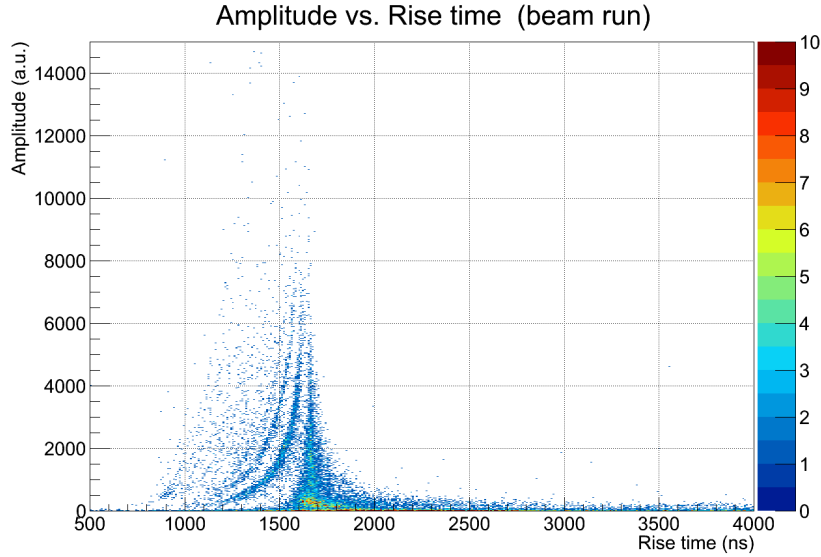


Figure 5.16: Amplitude versus rise time for gammas from a  $^{60}\text{Co}$  source. Both photopeaks are observable.

fast the energy is deposited on the crystal, while the slow one ( $N_s$ ) contains information about the total energy deposited in the crystal bulk. This way



*Figure 5.17:* Amplitude versus rise time for events registered when reaction was taking place. Different lines are found which correspond with different particles.

we obtain two parameters which can give us information about the nature of the particle entering the crystal. An example of this method is shown in figure 5.18.

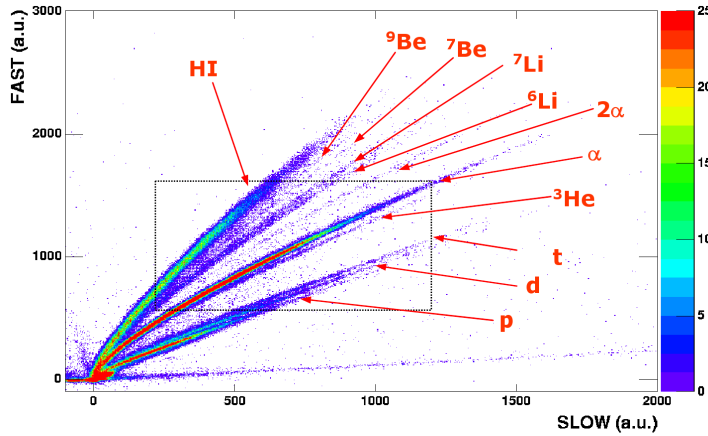


*Figure 5.18:* Fast versus Slow components. Taken from [32].

The output signal provided by the preamplifier is a convolution between the luminescence intensity  $L(t)$  and the impulse response of the preamplifier

$f(t) = e^{-\frac{t}{\tau_s}}$ , thereby the output signal is as follows

$$U(t) = (A + B)e^{-\frac{t}{\tau_p}} - Ae^{-\frac{t}{\tau_f}} - Be^{-\frac{t}{\tau_s}} \quad (5.16)$$

where  $A = \frac{N_f}{\frac{1}{\tau_f} - \frac{1}{\tau_p}}$  and  $B = \frac{N_s}{\frac{1}{\tau_s} - \frac{1}{\tau_p}}$ .

A complete mathematical explanation of the method is shown in Appendix B.

The first step is applying a Moving Window Deconvolution to  $U(t)$  with a gate length high enough to include all the original signal, in this case  $L_1 = 5\mu s$ . As a result we obtain a function  $Q(t)$

$$Q(t) = \tau_f N_f + \tau_s N_s - \tau_f N_f e^{-\frac{t}{\tau_f}} - \tau_s N_s e^{-\frac{t}{\tau_s}} ; \quad 0 \leq t \leq L_1 \quad (5.17)$$

where any contribution of the preamplifier has been removed (Appendix B.1). The point  $t = 0$  is defined as the point where traces take off, which can be different from one trace to next. Figure 5.19 shows how  $Q(t)$  looks after the MWD, in this case the timing origin is an arbitrary point.

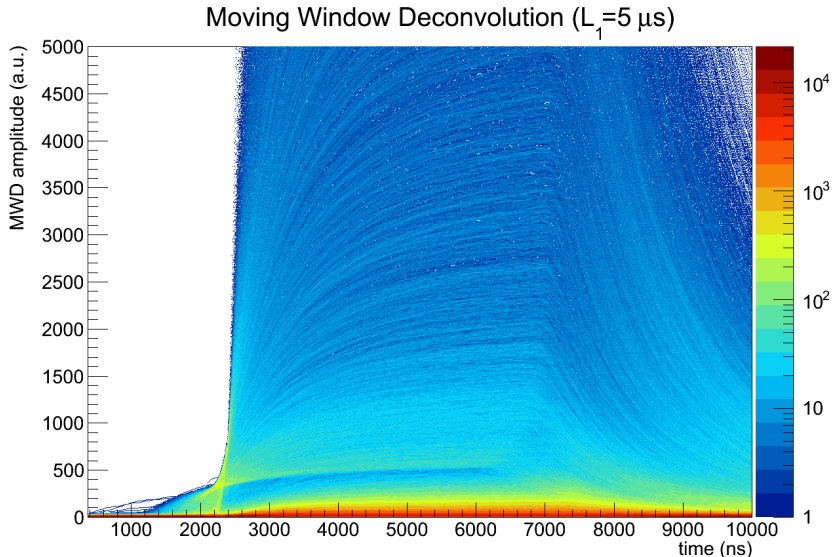


Figure 5.19: Signals after a Moving Window Deconvolution.

With the derivative of function (5.17) shown above,  $D(t) = \frac{dQ(t)}{dt}$  we obtain directly the luminescence function where we had started from

$$D(t) = N_f e^{-\frac{t}{\tau_f}} + N_s e^{-\frac{t}{\tau_s}} \quad (5.18)$$

A double exponential fit to these curves could give us quite good results, even though it is better going ahead with the analysis looking for more stable functions.

The next step is to multiply  $D(t)$  by  $e^{\frac{t}{\tau_s}}$ , resulting in

$$M(t) = N_s + N_f e^{-\frac{t}{\tau_{fs}}} \quad (5.19)$$

with  $\frac{1}{\tau_{fs}} = \frac{1}{\tau_f} - \frac{1}{\tau_s}$  (Appendix B.2). In figure 5.20 it is shown how signal traces look after each step, derivative and multiplication.

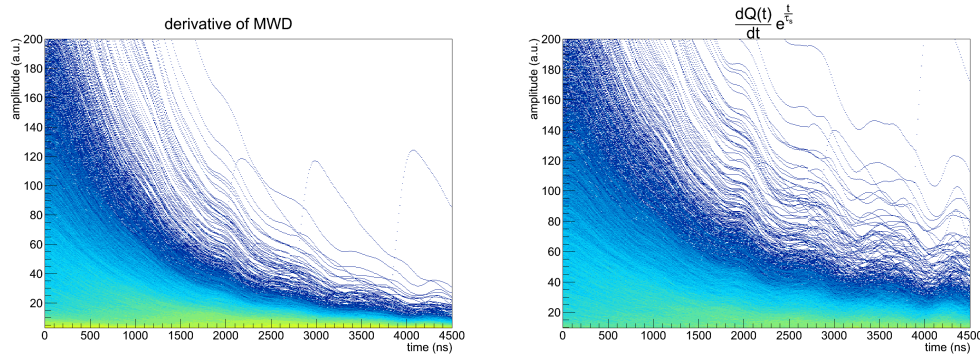


Figure 5.20: Signal traces after deriving process and multiplication.

The last step involves a second Moving Window Deconvolution, now with a gate length  $L_2 < L_1$  where two zones will be distinguished, the first one with a size  $0 < t < L_2$  and the other one with  $L_2 < t < L_1$ .

The new MWD is defined as follows

$$R(t) = M(t) - M(t - L_2) + \frac{1}{\tau_{fs}} \int_{t-L_2}^t M(t') dt' \quad (5.20)$$

the solutions for both zones are

$$\begin{aligned} R(t) &= N_f + N_s + \frac{N_s}{\tau_{fs}} t & 0 \leq t \leq L_2 \\ R(t) &= N_s \frac{L_2}{\tau_{fs}} & L_2 \leq t \leq L_1 \end{aligned} \quad (5.21)$$

The mathematical development of the second MWD is shown in appendix B.3.

For my analysis, the used length was  $L_2 = 2\mu s$  and the resulting traces are shown in Fig. 5.21.

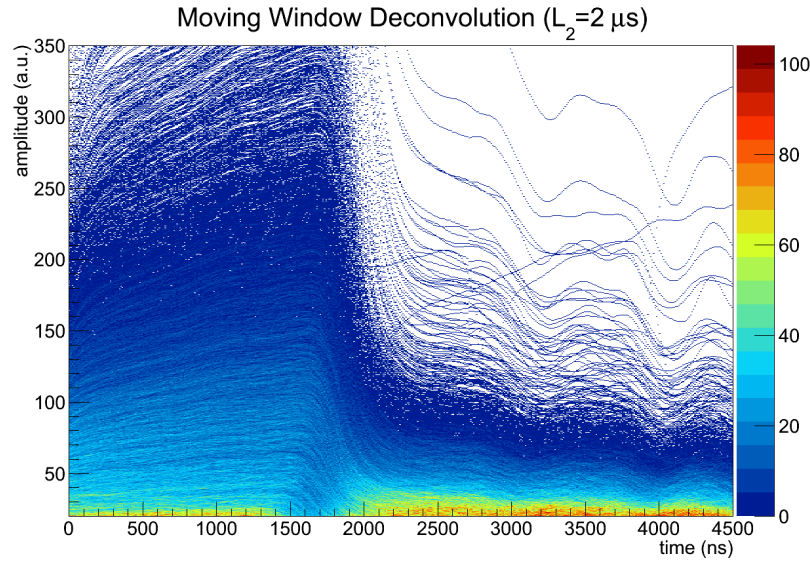


Figure 5.21: Resulting traces after all analysis process with two MWDs.

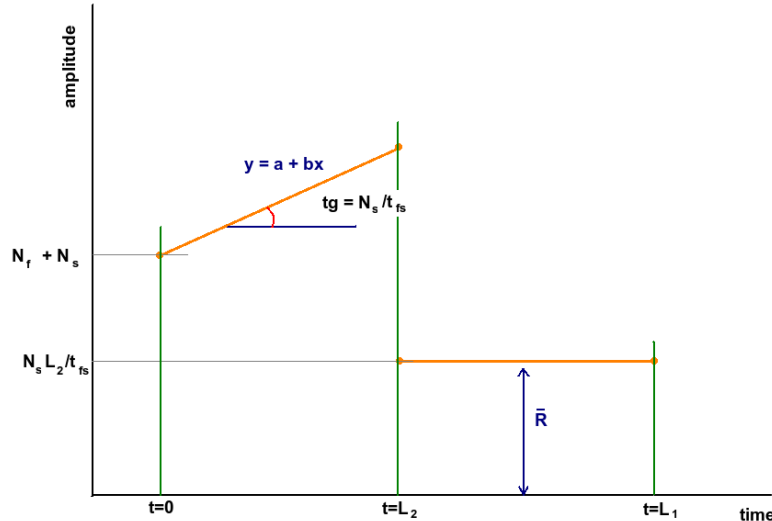


Figure 5.22: Schematic resulting shape of a trace.

From the first part of the trace we can obtain the *fast component* with a linear fit  $y = a + bx$  over this part, using the slope and the ordinate in the origin.

From the fit it is direct to find

$$N_f = a - \tau_{fs} b \quad (5.22)$$

From the second part, with the average value of the trace  $\bar{R}$  in this range, the *slow component* is found

$$N_s = \frac{\tau_{fs}}{L_2} \bar{R} \quad (5.23)$$

A schematic design is shown in Fig. 5.22, where both zones are plotted, the first with a straight line of slope  $N_s/t_{fs}$ , and the second one with a horizontal line.

Figures 5.23 and 5.24 reflect what we find when we compare the fast component against the slow one for the case of a  $^{60}\text{Co}$  source and for the case of events produced by the reaction trigger, where different particles are expected to reach the detector, respectively. A detailed analysis of these results will be shown in the next chapter.

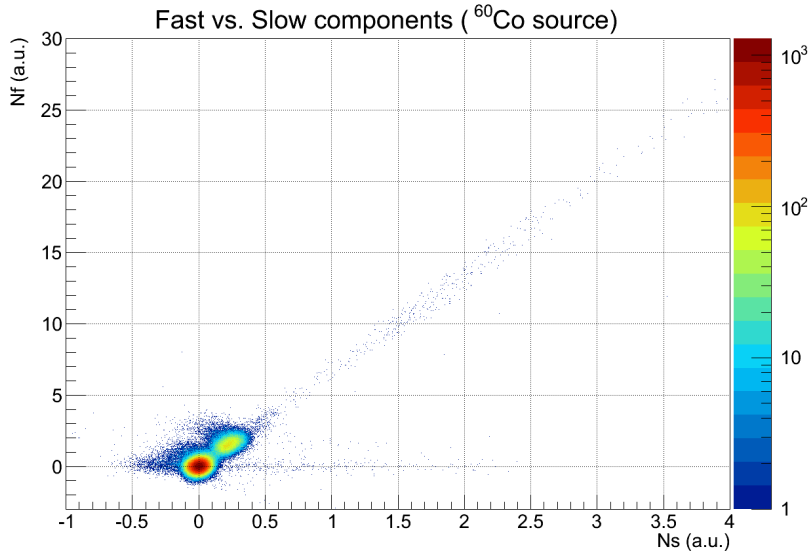


Figure 5.23: Fast vs. Slow component,  $^{60}\text{Co}$  source.

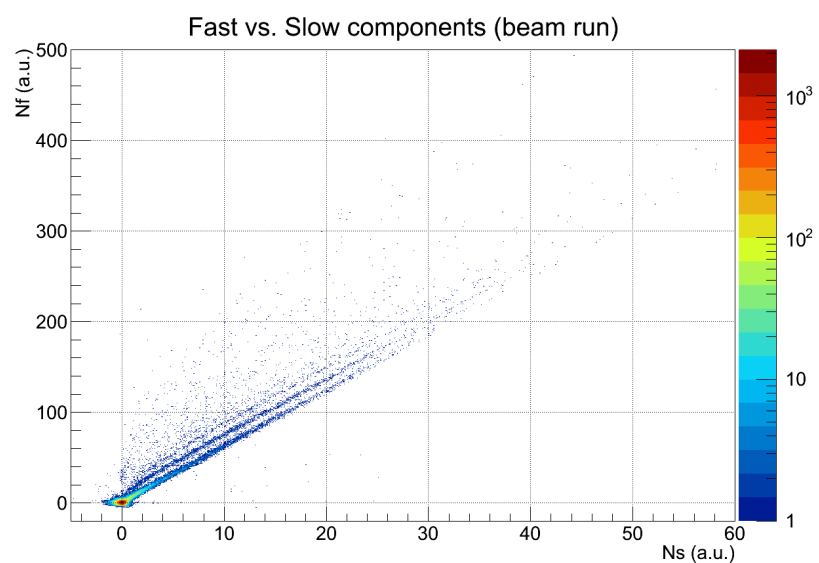


Figure 5.24: Fast vs. Slow component, run with beam.



# Chapter 6

## Results

In this chapter I will present the obtained results and how to interpret them in order to get particle identification. Results from using the signal rise time and fast and slow components will focus the discussion.

### Rise time

A direct simulation of the energy loss by charged particles when they pass through CsI gives us indicative information about the punch-through energy per type of particle. In this case the program used was *LISE++* [20]. The particles simulated were proton, deuterium, tritium,  $^3He$  and  $\alpha$ , and the resulting energies that they need to produce *punch-through* for a CsI crystal of 13 cm are presented in table 6.1.

Particle	$\Delta E_{CsI}$
p	231 MeV
d	306 MeV
t	362 MeV
$^3He$	831 MeV
$\alpha$	928 MeV

Table 6.1: Energy deposited in CsI crystal of 13 cm by charged particles just before *punching through*.

The energy loss for charged particles is obtained by using the energy

calibration done with the  $^{60}Co$  source. Particle identification can be achieved just by showing the relation between the energy loss and rise time.

A linear fit represent just a good approximation for energies in order of MeV, but not for higher energies. The method allows to identify the first line as protons which punch-through around 230 MeV (Fig. 6.1), being in good agreement with the real value of 231 MeV.

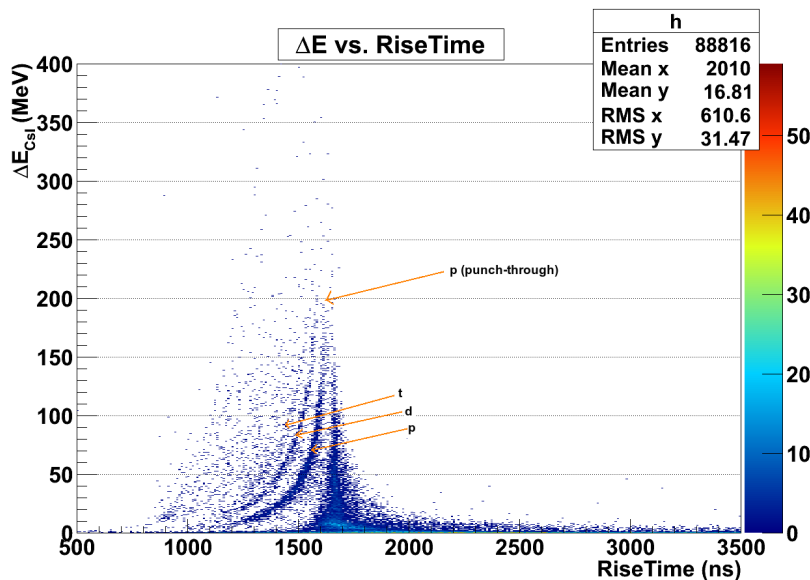


Figure 6.1: Graph of lost energy in the CsI crystal versus rise time for proton, deuterium and tritium identification. Punch-through point marked.

The second line is immediately identified as composed of deuterons, it is even possible to distinguish another line which would correspond to tritium. The punch-through point for deuterium and tritium lines are not found due to the low statistics in this region. Candidates for alphas and  $^3He$  are shown in Fig. 6.2, where the full energy range is plotted.

Unfortunately, the low He statistics available do prevent us from obtaining any conclusion in this identification capabilities.

For exploring the lowest energy zone, looking for gamma rays, another different preamplifier configuration should be used, where its range was reduced in a factor 10, becoming more sensitive to low energy events. With this configuration, and using the appropriate scaling factor, a region is found, between 0.5 MeV and 1.5 MeV, where  $\gamma$ -rays are found in the same region than  $^{60}Co$  shown in the last chapter. If it is true, those are expected to be photons from the decay of  $^{40}K$ . The acquisition trigger is fired by any crystal. This means that many times the event stored by one crystal is not

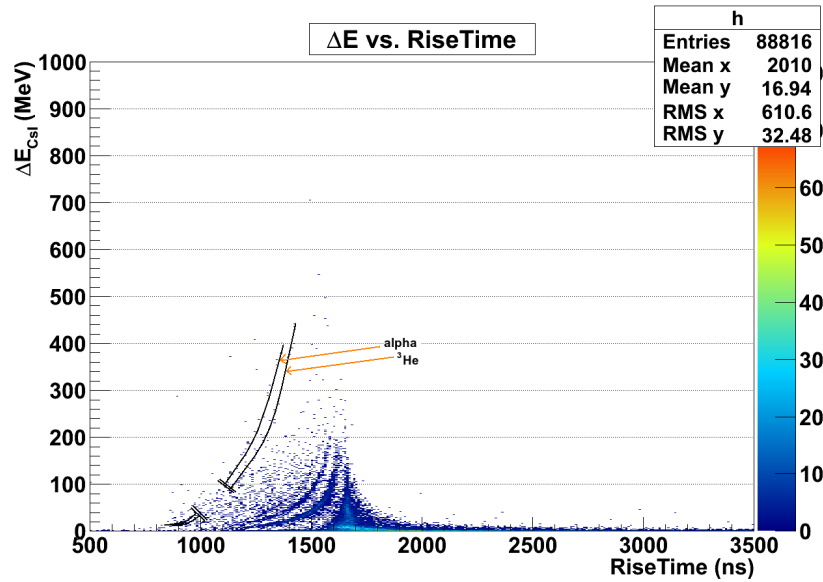


Figure 6.2: Graph of lost energy in the CsI crystal versus rise time for heavier ions identification.

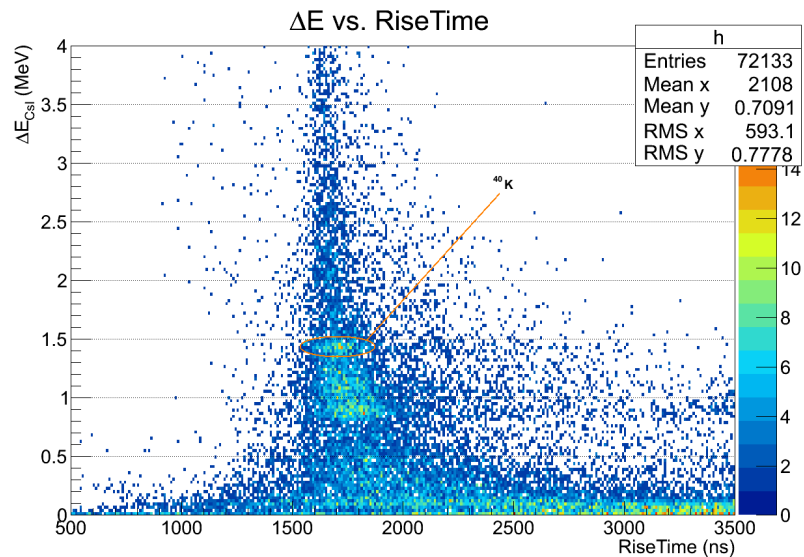


Figure 6.3: Graph of lost energy in the CsI crystal versus rise time for gamma rays identification.

correlated with the reaction, and background events are added to our spectrum. Furthermore, only a small amount of reaction events are stored due to dead time of our detector. These two facts make the 1.46 MeV peak from

$^{40}K$  accumulate, becoming visible. If we look at Fig. 6.3, where energy lost versus risetime are plotted, the photopeak of  $^{40}K$  can be seen, (surrounded by an ellipse).

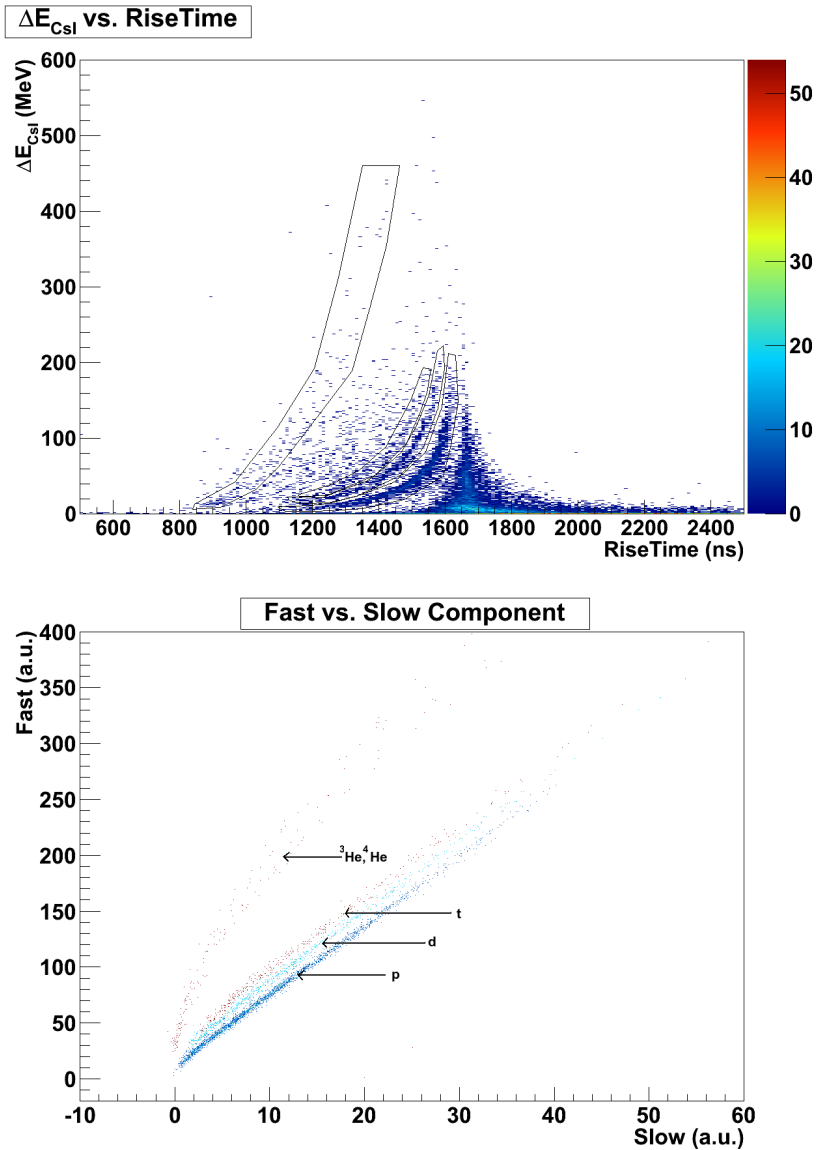


Figure 6.4: Cuts in  $\Delta E$  vs. RiseTime plot and their corresponding lines in Fast vs. Slow graph.

## Fast and Slow components

The results obtained using the fast and slow components method must be consistent with the results obtained with the rise time method. Once proton, deuterium and tritium are identified by the rise time method, individual cuts are done in each line. The correspondent events are shown in figure 6.4 for the fast-slow method. Well defined parallel lines are found for the three hydrogen isotopes. The helium candidates are also shown.

## Crosscheck

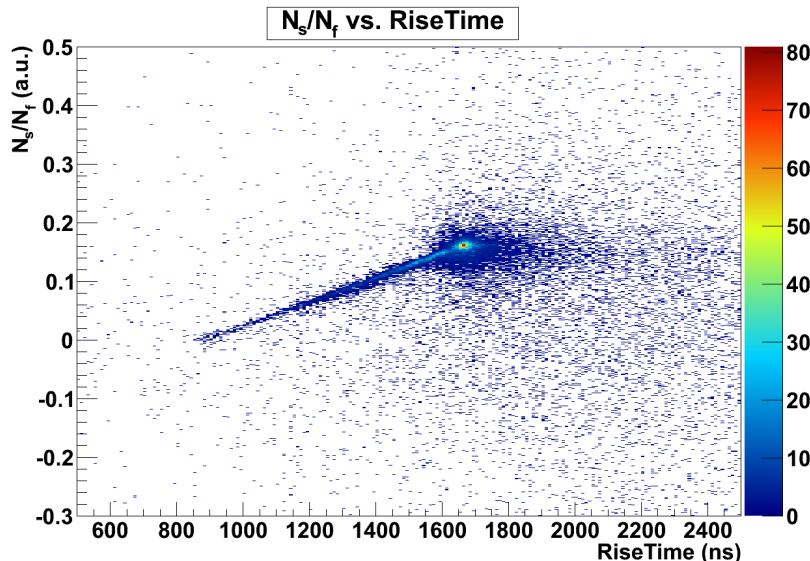


Figure 6.5: Linear correlation between the  $N_s/N_f$  fraction and Rise time.

Once we know which line corresponds to which particle, it is interesting to see how good is the relative separation for different particles. The slow component ( $N_s$ ) is proportional to the signal amplitude and the fast component ( $N_f$ ) is associated with how fast the signal rises. The ratio  $N_s/N_f$  must be directly related with the Rise time, being this relation experimentally observed to be linear (Fig. 6.5). There are many counts that do not keep this linear relation, although they might probably be irrelevant, but they might be caused by electronic noise or failures in the methods. The Fast vs. Slow component graph, taking into account only well-correlated events, is shown in figure 6.6, where apart from the lines explained before, there is one first line corresponding to gamma rays and light charged particles after punching through.

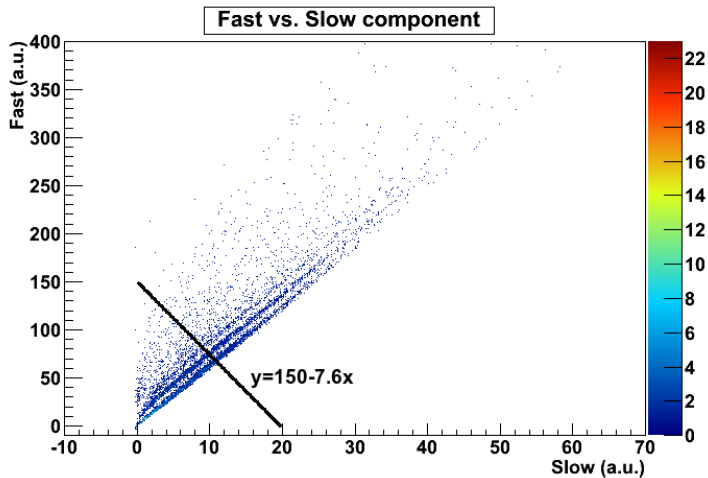


Figure 6.6: Fast vs. Slow component representation after the filter of Rise-Time vs.  $N_f/N_s$  correlation. The line used for the projection is shown.

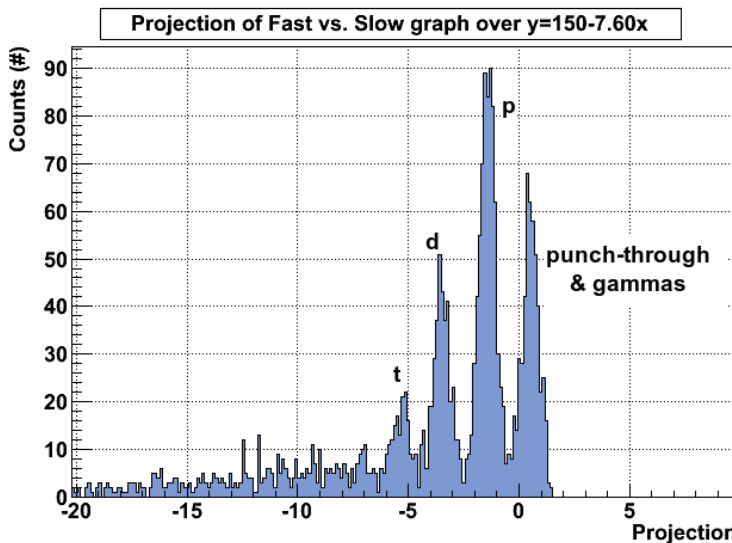


Figure 6.7: Particle identification plot from the previous projection. Tritium is clearly seen in this plot.

Projecting onto a set of axes perpendicular to the lines defined by each particle type, it is possible to obtain the cleanest particle separation. With this projection, we can confirm the identification of the tritium. Figure 6.7 shows the result of the projection.

# Chapter 7

## Summary and Conclusions

In this chapter, a brief summary of the work and the most relevant conclusions obtained from the analysis are presented.

### Summary

The analysis performed in this work was focused on testing the identification capability of light charged particles and gammas by a prototype of the calorimeter CALIFA, ProtoZero, as well as to check the energy resolution for gammas and the capability of different PID methods. For these purposes I have been working with data from an experiment that took place at GSI where the ProtoZero was part of the ASY-EOS detector setup.

The study of energy resolution was carried out by two different methods, an offline analysis based on a Moving Window Deconvolution and an online hardware analysis based on the trapezoidal FIR filter.

A pulse shape analysis allowed to achieve particle identification. Two techniques were used in this work, the first one is based on the signal rise time, and the second one is based on the two components, fast and slow, of the primordial signal. For this latter case, a wide shape analysis was needed to depurate the signal.

For the gamma ray study, a new configuration in electronics was needed, the range in gain of the preamplifier was reduced by a factor 10. With this new range, and therefore with better sensitivity, the region of few MeV gammas was clearly reached in comparison to  $^{60}\text{Co}$ .

The lack of energetic heavier ions such as alpha particles could be explained by the large angle between the beam line axis and the detector position. With projectiles as fast as in this experiment, 400 AMeV  $^{197}\text{Au}$ , ions heavier than hydrogen are likely forced to go forward, reducing the probability of being detected by our prototype.

## Conclusions

- Energy resolutions for  $^{60}Co$  gammas of 4.94% and 4.74% were achieved via software analysis. The hardware FIR filter reaches resolutions of 4.70% and 4.52% for the same peaks.
- Pulse shape analysis shows the high identification capability of the crystals. Identification of light charged particles such as protons, deuterium and tritium as well as gammas was achieved.
- Two methods, rise time and fast-slow components, were tested and compared to each other. Better identification results were obtained with the fast-slow components method.
- The combination of the CsI crystals with the proposed electronics and the tested pulse shape algorithms implemented have proved to be suitable for high energy resolution and high PID capability.

## Appendix A

# Moving Window Deconvolution Calculations

The preamplifier impulse response  $f(n)$  is assumed to be a exponential decay  $f(n) = k^n$  where  $k = e^{-\frac{1}{\tau_p}}$ . The preamplifier output  $U_p(n)$  is the convolution of the original signal  $g(n)$  with the preamplifier impulse response  $f(n)$ :

$$U_p(i) = \sum_{j=z}^i g(j)f(i-j) ; \quad i > z \quad (\text{A.1})$$

$g(n)$  is obtained as follows

$$\begin{aligned} U_p(n) &= \sum_{j=n-L}^n g(j)k^{n-j} = k \cdot \sum_{j=n-L}^n g(j)k^{n-1-j} = \\ &g(n) + k \cdot \sum_{j=n-L}^{n-1} g(j)k^{n-1-j} = g(n) + kU_p(n-1) \end{aligned} \quad (\text{A.2})$$

$$g(n) = U_p(n) - kU_p(n-1) \quad (\text{A.3})$$

With the definition of integrated charge

$$G(n) = \sum_{j=n-L}^n g(j) \quad (\text{A.4})$$

we find the equation used in the MWD method as

$$G(n) = \sum_{j=n-L}^n (U_p(j) - kU_p(j-1)) = \sum_{j=n-L}^n U_p(j) - k \cdot \sum_{j=n-L}^n U_p(j-1) \quad (\text{A.5})$$

using

$$\sum_{j=n-L}^n U_p(j) = U_p(n) + \sum_{j=n-L}^{n-1} U_p(j) \quad (\text{A.6})$$

and

$$\sum_{j=n-L}^n U_p(j-1) = \sum_{j=n-L-1}^{n-1} U_p(j) = U_p(n-L-1) + \sum_{j=n-L}^{n-1} U_p(j) \quad (\text{A.7})$$

we obtain

$$G(n) = U_p(n) - kU_p(n-L-1) + (1-k) \cdot \sum_{j=n-L}^{n-1} U_p(j) \quad (\text{A.8})$$

with

$$\begin{aligned} kU_p(n-L-1) &= \sum_{j=z_0}^{n-L-1} g(j)k^{n-L-j} = \\ &\sum_{j=z_0}^{n-L} g(j)k^{n-L-j} - g(n-L) = U_p(n-L) - g(n-L) \end{aligned} \quad (\text{A.9})$$

so at the end

$$G(n) = U_p(n) - U_p(n-L) + (1 - e^{-\frac{1}{\tau_p}}) \sum_{n-L}^{n-1} U_p(j) + g(n-L) \quad (\text{A.10})$$

The component  $g(n-L)$  in the last equation is removed along this work because we can assume that it is always zero for all the range of interest in  $n$  which extends from zero to  $n = L$ . It is important to remove the *baseline* in this case.

## Appendix B

# Calculations for Fast and Slow components deduction

If we parametrize the crystal's luminescence as a sum of two decay exponential functions

$$L(t) = N_f e^{-\frac{t}{\tau_f}} + N_s e^{-\frac{t}{\tau_s}} \quad (\text{B.1})$$

the output signal after the preamplifier will be a convolution of this luminescence function and the preamplifier impulse response  $f(t) = e^{-\frac{t}{\tau_p}}$

$$\begin{aligned} U(t) &= \int_0^t (N_f e^{-\frac{t'}{\tau_f}} + N_s e^{-\frac{t'}{\tau_s}}) \cdot e^{-\frac{t-t'}{\tau_p}} \cdot dt' \\ &= \left( \frac{N_f}{\frac{1}{\tau_f} - \frac{1}{\tau_p}} + \frac{N_s}{\frac{1}{\tau_s} - \frac{1}{\tau_p}} \right) e^{-\frac{t}{\tau_p}} - \frac{N_f}{\frac{1}{\tau_f} - \frac{1}{\tau_p}} e^{-\frac{t}{\tau_f}} - \frac{N_s}{\frac{1}{\tau_s} - \frac{1}{\tau_p}} e^{-\frac{t}{\tau_s}} \end{aligned} \quad (\text{B.2})$$

$U(t)$  is the input for the development shown in the next three points. In section B.1, the integrated charge function is obtained. In section B.2, this integrated charge is time-derivated and multiplied by  $e^{\frac{t}{\tau_s}}$ , looking for a function more suitable for the next step. In point B.3, the last function is processed by a second MWD, which allows to obtain  $N_f$  and  $N_s$ .

### B.1 MWD with length $L_1$

The output signal becomes more manageable by using:

$$\begin{aligned} A &= \frac{N_f}{\frac{1}{\tau_f} - \frac{1}{\tau_p}} \\ B &= \frac{N_s}{\frac{1}{\tau_s} - \frac{1}{\tau_p}} \end{aligned} \quad (\text{B.3})$$

and, in this way

$$U(t) = (A + B)e^{-\frac{t}{\tau_p}} - Ae^{-\frac{t}{\tau_f}} - Be^{-\frac{t}{\tau_s}} \quad (\text{B.4})$$

Now we apply the MWD to our output signal

$$Q(t) = U(t) - U(t - L_1) + (1 - e^{-\frac{1}{\tau_p}}) \int_{t-L_1}^t U(t') dt' \quad (\text{B.5})$$

it was proved that  $\tau_p$  is higher than any other time constant, so in our scale  $\frac{1}{\tau_p}$  is small enough for using the next approximation

$$e^{-\frac{1}{\tau_p}} \simeq 1 - \frac{1}{\tau_p} \quad (\text{B.6})$$

Furthermore, our range of interest is extended to  $0 < t < L_1$  and as we know  $U(t)$  is null for all times less than zero

$$\begin{aligned} U(t') &= 0 \quad \forall t' \quad / \quad t - L_1 \leq t' \leq 0 \\ \int_{t-L_1}^t U(t') dt' &= \int_{t-L_1}^0 U(t') dt' + \int_0^t U(t') dt' = \int_0^t U(t') dt' \end{aligned} \quad (\text{B.7})$$

This way, the MWD function is obtained as follows

$$\begin{aligned} Q(t) &= U(t) + \frac{1}{\tau_p} \int_0^t U(t') dt' = \\ (A + B)e^{-\frac{t}{\tau_p}} - Ae^{-\frac{t}{\tau_f}} - Be^{-\frac{t}{\tau_s}} &+ \frac{1}{\tau_p} \int_0^t \left[ (A + B)e^{-\frac{t'}{\tau_p}} - Ae^{-\frac{t'}{\tau_f}} - Be^{-\frac{t'}{\tau_s}} \right] dt' \end{aligned} \quad (\text{B.8})$$

$$Q(t) = \tau_f N_f + \tau_s N_s - \tau_f N_f e^{-\frac{t}{\tau_f}} - \tau_s N_s e^{-\frac{t}{\tau_s}} ; \quad 0 \leq t \leq L_1 \quad (\text{B.9})$$

## B.2 Derivative of MWD ( $L_1$ ) and multiplication by $e^{\frac{t}{\tau_s}}$

A more suitable equation is obtained with the temporal derivative of the equation (B.9) as follows:

$$D(t) = \frac{dQ(t)}{dt} \quad (\text{B.10})$$

$$D(t) = N_f e^{-\frac{t}{\tau_f}} + N_s e^{-\frac{t}{\tau_s}} \quad (\text{B.11})$$

The exponential terms are reduced to one by multiplying the last equation by  $e^{\frac{t}{\tau_s}}$

$$M(t) = D(t) e^{\frac{t}{\tau_s}} \quad (\text{B.12})$$

$$M(t) = N_s + N_f e^{-t(\frac{1}{\tau_f} - \frac{1}{\tau_s})} = N_s + N_f e^{-\frac{t}{\tau_{fs}}} \quad (\text{B.13})$$

where  $\frac{1}{\tau_{fs}} = \frac{1}{\tau_f} - \frac{1}{\tau_s}$

This last equation is the appropriate for a second MWD.

### B.3 MWD with length $L_2 < L_1$

Two simple geometrical relationships are found for obtaining  $N_f$  and  $N_s$  by applying a second MWD to the equation (B.13):

$$R(t) = M(t) - M(t - L_2) + \frac{1}{\tau_{fs}} \int_{t-L_2}^t M(t') dt' \quad (\text{B.14})$$

We must distinguish between two different ranges,  $0 \leq t \leq L_2$  and  $L_2 \leq t \leq L_1$ .

For  $0 \leq t \leq L_2$ :

$$\begin{aligned} M(t') &= 0 \quad \forall t' \quad / \quad t - L_2 \leq t' \leq 0 \\ \int_{t-L_2}^t M(t') dt' &= \int_{t-L_2}^0 M(t') dt' + \int_0^t M(t') dt' = \int_0^t M(t') dt' \end{aligned} \quad (\text{B.15})$$

$$R(t) = M(t) + \frac{1}{\tau_{fs}} \int_0^t M(t') dt' = N_s + N_f e^{-\frac{t}{\tau_{fs}}} + \frac{1}{\tau_{fs}} \int_0^t \left[ N_s + N_f e^{-\frac{t'}{\tau_{fs}}} \right] dt' \quad (\text{B.16})$$

For  $L_2 \leq t \leq L_1$ :

$$R(t) = N_s + N_f e^{-\frac{t}{\tau_{fs}}} - \left( N_s + N_f e^{-\frac{t-L_2}{\tau_{fs}}} \right) + \frac{1}{\tau_{fs}} \int_{t-L_2}^t \left[ N_s + N_f e^{-\frac{t'}{\tau_{fs}}} \right] dt' \quad (\text{B.17})$$

as a result, we obtain

$$\begin{aligned} R(t) &= N_f + N_s + \frac{N_s}{\tau_{fs}} t & 0 \leq t \leq L_2 \\ R(t) &= N_s \frac{L_2}{\tau_{fs}} & L_2 \leq t \leq L_1 \end{aligned} \quad (\text{B.18})$$



# Bibliography

- [1] GENP, <http://www.usc.es/genp>
- [2] GSI, <http://www.gsi.de>
- [3] W. R. Leo, “Techniques for Nuclear and Particle Physics Experiments”, Springer-Verlag, 1994, Berlin.
- [4] Glenn F. Knoll, “Radiation Detection and Measurement”, John Wiley & Sons, Inc., 2000, New York.
- [5] H. Alvarez-Pol et al. “Design studies and first crystal test for the R<sup>3</sup>B calorimeter” Nucl. Instr. and Meth. B, 266 (2008) 4616-4620.
- [6] W. Skulski and M. Momayezi, “Particle identification in CsI(Tl) using digital pulse shape analysis” Nucl. Instr. and Meth. A, 458 (2001) 759-771.
- [7] M. Gascón et al. “Test of LAAPDs coupled to CsI(Tl) Crystals for the CALIFA R<sup>3</sup>B/FAIR calorimeter.
- [8] M. Moszyński et al. “Particle identification by digital charge comparison method applied to CsI(Tl) crystal coupled to photodiode”, Nucl. Instr. and Meth. A, 336 (1993) 587-590.
- [9] M. Moszyński “Inorganic scintillation detectors in  $\gamma$ -ray spectrometry” Nucl. Instr. and Meth. A, 505 (2003) 101-110.
- [10] M. Winkel et al. “CALIFA ProtoZero Test” Private communication, 2011.
- [11] PDG book, <http://pdg.lbl.gov>
- [12] M. Mostazo “Pulse-shape analysis of signals from scintillators irradiated by high-energy gamma photons and light charged particles.” Master thesis, 2010.

- [13] M.Gascón “Prototype of a new calorimeter for the studies of nuclear reactions with relativistic radioactive beams” PhD thesis, 2010.
- [14] M. Bendel, “Entwicklung und Test einer digitalen Auslese für das CALIFA-Kalorimeter”, Diploma thesis, 2010.
- [15] V. Avdeichikov et al. “Energy calibration of CsI(Tl) scintillator in pulse-shape identification technique” Nucl. Instr. and Meth. A, 501 (2003) 505-513.
- [16] <http://www.mesytec.com>
- [17] MPRB-16 16 Channel Preamplifier, Data Sheet.
- [18] <http://www.struck.de/sis3302.htm>
- [19] “SIS3302 100 MHz 16-bit VME Digitizer” User manual, SIS Documentation.
- [20] “LISE tutorial” <http://www.nscl.msu.edu/lise>
- [21] A. Syntfeld-Kažuch et al. “Light pulse shape Dependence on  $\gamma$ -ray energy in CsI(Tl)”, IEE Transactions on Nuclear Science, 55, No.3 (2008)
- [22] A. Pagano et al. “Physics with the Chimera detector at LNS in Catania: The RESERVE experiment” Nuclear Physics A, 681 (2001) 331c-338c.
- [23] J.D. Valentine et al. “Temperature dependence of CsI(Tl) gamma-ray excited scintillation characteristics”, Nucl. Instr. and Meth. A, 325 (1993) 147-157.
- [24] A.Georgiev and W. Gast, “Digital Pulse Processing in High Resolution, High Throughput Gamma-Ray Spectroscopy” IEE Transactions on Nuclear Science, 40, No.4 (1993).
- [25] P. Marchand and L. Marmet, “Binomial smoothing filter: A way to avoid some pitfalls of least-squares polynomial smoothing” Rev. Sci. Instrum. 54 (1983) 8.
- [26] B.W.Loo and F.S. Goulding, “Ballistic deficits in pulse shaping amplifiers”, IEEE Transactions on Nuclear Science, 35, No.1 (1988).
- [27] T.A. DeVol et al. “Dual parameter analysis of CsI:Tl/PMT with a digital oscilloscope”, Nucl. Instr. and Meth. A, 435 (1999) 433-436.

- [28] A. Georgiev et al. “An Analog-to-Digital conversion based on a Moving Window Deconvolution”, IEEE Transactions on Nuclear Science, 41, No.4 (1994).
- [29] J. Gál et al. “Optimization of the particle discriminator based on the ballistic deficit method using delay-switched gated integrator”, Nucl. Instr. and Meth. A, 399 (1997) 407-413.
- [30] J. Gál et al. “Particle discriminator for the identification of light charged particles with CsI(Tl) scintillator + PIN photodiode detector”, Nucl. Instr. and Meth. A, 366 (1995) 120-128.
- [31] P. Russotto, “XCVI Congresso Nazionale”, Bologna, Sep. 2010.
- [32] P. Guazzoni, “IWM2007-GANIL”.
- [33] FIR filters, Connexions, <http://cnx.org/content/m12009/latest/>
- [34] Convolution properties, Connexions, <http://cnx.org/content/m12829/latest/>
- [35] F. Benrachi et al. “Investigation of the performance of CsI(Tl) for charged particle identification by pulse-shape analysis”, Nucl. Instr. and Meth. A, 281 (1989) 137-142.
- [36] J. Stein et al. “X-ray detectors with digitized preamplifiers”, Nucl. Instr. and Meth B, 113 (1996) 141-145.
- [37] The ROOT team, “ROOT Users Guide 5.30”, 2011